

Ion-ion cross-field instability of lower hybrid waves in the inner coma of comet 67P

Elias Odelstad¹, Tomas Karlsson², Anders Eriksson¹, Sofia Bergman³,
Gabriella Stenberg Wieser³

¹Swedish Institute of Space Physics

²KTH Royal Institute of Technology

³Swedish Institute of Space Physics, Kiruna, Sweden

¹Uppsala, Sweden

²Stockholm, Sweden

Key Points:

- Pick-up ions and locally produced cometary ions co-occur in the inner coma, with strong relative streaming motion.
- An ion-ion cross-field instability is likely to develop as a result of the relative streaming motion.
- This instability is probably responsible for generating at least some of the lower hybrid waves observed at the comet.

Abstract

We show that an ion-ion cross-field streaming instability between cold newborn cometary ions and heated heavy ions that were picked up upstream is likely a contributing source of observed lower hybrid (LH) waves in the inner coma of comet 67P/Churyumov-Gerasimenko. Electric field oscillations in the LH frequency range are common here, and have previously been attributed mainly to the lower-hybrid drift instability (LHDI), driven by gradients associated with observed local density fluctuations. However, the observed wave activity is not confined to such gradients, nor is it always strongest there. Thus, other instabilities are likely needed as well to explain the observed wave activity. Several previous works have shown the existence of multiple populations of cometary ions in the inner coma of 67P, distinguished by differences in mass, energy and/or flow direction. We here examine two selected time intervals in October and November 2015, with substantial wave activity in the lower hybrid frequency range, where we identify two distinct cometary ion populations: a bulk population of locally produced, predominantly radially outflowing ions, and a more tenuous population picked up further upstream and accelerated back towards the comet by the solar wind electric field. These two populations exhibit strong relative drifts (~ 20 km/s, or about 5 times the pickup ion thermal velocity), and we perform an electrostatic dispersion analysis showing that conditions should be favorable for lower hybrid wave generation through the ion-ion cross-field instability.

1 Introduction

1.1 Comets as natural laboratories for space plasma measurements

The neutral gas coma of an active comet is subject to ionization by solar EUV radiation (as well as charge exchange and electron impact reactions with the solar wind and high-energy electrons, see for example Cravens, 1991). It thus provides an extended source of newly ionized plasma to the surrounding interplanetary medium, otherwise dominated by the solar wind (hereafter SW). The resulting interaction between SW and cometary plasma (e.g. Neugebauer, 1990) gives rise to an abundance of plasma instabilities, waves and turbulent phenomena (Tsurutani, 1991). The cometary plasma environment therefore provides an excellent setting for studying such processes, which often play important roles in the physics and dynamics of plasmas. For example, they can heat or cool plasma populations, produce supra-thermal electrons, reduce plasma anisotropies and gradients, couple different plasma species to each other, and provide anomalous resistivity.

1.2 The Rosetta mission

The European Space Agency's Rosetta mission (Glassmeier, Boehnhardt, et al., 2007; Taylor et al., 2017) brought a spacecraft to the comet 67P/Churyumov-Gerasimenko (hereafter 67P), following it in its orbit around the Sun from August 2014 (at 3.6 au from the Sun) through perihelion in August 2015 (at 1.24 au) until the end of September 2016 (3.8 au). The instruments of the Rosetta Plasma Consortium (RPC) (Carr et al., 2007) thus got an unprecedented long-term view of the near-nucleus cometary plasma environment of an intermediately active comet, for which the production rate varied between $\sim 4 \cdot 10^{25} \text{ s}^{-1}$ and $\sim 3.5 \cdot 10^{28} \text{ s}^{-1}$ during the mission (Hansen et al., 2016; Heritier et al., 2017). The spacecraft mostly stayed in close to terminator orbit within about 400 km of the nucleus (with the exception of two brief ($\lesssim 1$ month) sunward and tailward excursions to beyond ~ 1000 km).

1.3 Plasma waves at comets

Previous comets subject to in situ measurements of plasma waves (21P/Giacobini-Zinner, 1P/Halley and 26P/Grigg-Skjellerup) all exhibited very strong hydromagnetic

turbulence in the ultralow-frequency (ULF) range, $f < 1$ Hz in the spacecraft (S/C) frame, with maximum power near the local water ion cyclotron frequency ($\sim 10^{-2}$ Hz) (Tsurutani et al., 1995). This was attributed to instabilities caused by the highly anisotropic velocity distribution of the newly born cometary ions in the SW frame. They essentially form a ring, beam or combined “ring-beam” distribution in velocity space depending on the angle between the interplanetary magnetic field and the SW velocity, which can lead to the generation of a multitude of ULF instabilities (Tsurutani, 1991). The resulting waves then act back on the particle distribution, e.g. causing pitch angle scattering, and thus play an important role in the process of incorporating the newly picked up cometary ions into the SW flow (Coates, 2004).

Plenty of plasma waves were also detected at higher frequencies, in the ELF (1–1,500 Hz) and VLF (10^3 – 10^6 Hz) ranges (Scarf, 1989; Laakso, 1991). These included ion acoustic waves ($0.6 < f < 10$ kHz), electron plasma oscillations ($f \gtrsim 10^4$ Hz), electromagnetic waves at frequencies characteristic of the electron-scale whistler mode ($f \lesssim 100$ Hz) and near the hydrogen lower-hybrid frequency (6–12 Hz) (Scarf et al., 1986; Galeev et al., 1988). The last one has been proposed to be generated by an ion-loss cone instability, also caused by the pick-up of water group cometary ions into a perpendicular ring distribution (Coroniti et al., 1986). The whistler waves were thought to be excited by supra-thermal electrons accelerated by the lower-hybrid waves (Galeev, 1987).

1.4 Waves at 67P

Contrary to earlier cometary spacecraft encounters, at 67P the gyro-radius of newborn cometary ions was typically much larger than the scale size of the innermost interaction region, where Rosetta spent almost all of its time. Therefore, the ring-beam type pick-up distributions characterizing previous encounters did generally not develop here (Behar et al., 2017). Yet, many different kinds of plasma waves have been observed at 67P. Low-frequency, large-amplitude ($\delta B/B \sim 1$) compressional magnetic field oscillations at ~ 20 –50 mHz (a.k.a. “singing comet waves”) were observed in the early and late low-activity phases of the mission, disappearing during the high-activity phase between March 2015 and Spring 2016 (Richter et al., 2015, 2016; Breuillard et al., 2019; Goetz et al., 2020). These have been proposed to be generated by a modified ion-Weibel instability driven by the cross-field current between the essentially unmagnetized cometary ions and the magnetized electrons (Meier et al., 2016).

Plasma density oscillations at frequencies ~ 200 Hz attributed to ion acoustic waves were observed both in the magnetized plasma in the early low-activity phase (Gunell, Nilsson, et al., 2017) and in the unmagnetized plasma inside the diamagnetic cavity (Goetz, Koenders, Richter, et al., 2016; Goetz, Koenders, Hansen, et al., 2016) during the high-activity phase close to perihelion (Gunell, Goetz, et al., 2017). A current-driven instability was proposed to generate these waves, at least inside the cavity, but the exact nature of the instability has not yet been addressed.

Mirror mode waves have also been reported at 67P by Volwerk et al. (2016). These were proposed to have been generated by unstable ring-beam type pick-up ion distributions of the same kind as observed at previous comets. Such distributions were thus inferred to have developed also at 67P, although presumably limited to the heavily mass-loaded plasma and piled-up magnetic field in the inner coma close to perihelion where these waves were observed. Observations of energy-angle dispersion of accelerated heavy ions by Nicolaou et al. (2017) lends some credence to this hypothesis, although the ion gyro-motion would likely be more complex than for the classical ring or partial-ring distributions since the plasma here exhibits substantial inhomogeneities on spatial scales comparable to the local ion gyro-radii. Odelstad et al. (2020) reported ion Bernstein waves detected in the region surrounding the diamagnetic cavity, which were attributed to a similar instability.

1.5 Electric-field observations of waves at 67P

The first electric field measurements from 67P were presented by Karlsson et al. (2017), from deep within the coma in October and November 2015, close to peak activity of the comet. Persistent wave activity near the local H_2O^+ lower hybrid frequency was observed, and the largest amplitudes were found at or near pronounced plasma density gradients. The lower hybrid drift instability (LHDI) was thus proposed as the generation mechanism for these waves. André et al. (2017) further explored this possibility using numerical solutions of the relevant dispersion relations, finding that, unless the electron motion is significantly interrupted by collisions with neutrals, large local density gradients are often favourable for the generation of lower hybrid waves by the LHDI in the near-nucleus plasma. Later in the mission, when solar wind protons were observed in the inner coma, Goldstein et al. (2019) showed that conditions were favourable for a two-stream instability between these and picked-up cometary water ions to develop, also generating waves in the lower-hybrid frequency range.

Madsen et al. (2018) also observed electrostatic waves in the lower-hybrid frequency range inside the diamagnetic cavity of 67P, which they interpreted as ion acoustic waves excited by the forcing on the cavity boundary by lower hybrid waves in the surrounding magnetized plasma.

Lower hybrid waves can energize both electrons and ions through Landau-Cherenkov resonance acceleration (Bingham et al., 2002). This has been suggested as the mechanism responsible for accelerated electrons at 67P reported by e.g. Clark et al. (2015), Broiles, Livadiotis, et al. (2016); Broiles, Burch, et al. (2016) and Goldstein et al. (2019).

In this study, we expand and build upon the results of previous authors by considering another possible source of wave growth in the lower hybrid frequency range in the inner plasma environment of 67P; an instability due to opposite flows of streaming ions across the magnetic field.

2 Instrumentation and data

Rosetta carried a collection of five plasma instruments (Carr et al., 2007). In this study, we focus on data from the Langmuir probe instrument (LAP) and Ion Composition Analyser (ICA), and rely on the Fluxgate Magnetometer (MAG) and Mutual Impedance Probe (MIP) for supporting magnetic field and plasma density data, respectively.

2.1 The Langmuir probe instrument (RPC-LAP)

LAP (Eriksson et al., 2007) comprises two spherical Langmuir probes (LAP1 and LAP2), 5 cm in diameter, mounted on booms of 2.24 and 1.6 m lengths, respectively. (See e.g. Figure 1 in Karlsson et al. (2017) for the detailed geometric configuration.) The instrument is capable of three basic modes of operation: current measurements at fixed bias potential, potential measurements at fixed bias current (or with a floating probe, i.e., disconnected from the biasing circuitry) and Langmuir probe bias potential sweeps. In this paper, we exclusively use data from the second mode with floating probes. This is the appropriate configuration for electric field measurements in moderate to high density ($\gtrsim 10^2 \text{ cm}^{-3}$) space plasmas (Maynard, 1998). We use data obtained with burst telemetry rate, in which 20-bit data is acquired at a sample rate of 57.8 Hz, sufficient to resolve waves in the lower-hybrid frequency range ($\sim 1\text{--}10 \text{ Hz}$). Such double-probe electric field measurements were only collected intermittently, unevenly distributed over the mission but often at least 8–12 h/week.

From the two individual probe potentials two important physical parameters can be obtained, or at least estimated: the electrostatic potential of the spacecraft w.r.t. the ambient plasma ($V_{S/C}$) and the electric field component along the direction of separa-

tion of the two probes. In the ideal case, when the boom lengths far exceed the Debye length, each probe potential (measured w.r.t. the spacecraft, which is the floating ground of the measurements) would correspond to the negative of the spacecraft potential, with an additive offset due to the floating potential of the probe w.r.t. the plasma (Odelstad et al., 2017). In the presence of an ambient electric field \mathbf{E} , the plasma potentials at the locations of the two probes will differ by a quantity $\mathbf{E} \cdot \mathbf{d}$, where $\mathbf{d} = \mathbf{r}_{\text{LAP1}} - \mathbf{r}_{\text{LAP2}}$ is the probe separation vector. If the perturbation due to the electric field is small, so that the probe floating potential doesn't change, the potential difference between the probes will simply equal $\mathbf{E} \cdot \mathbf{d}$, from which the electric field component along \mathbf{d} can be obtained.

These measurements are complicated by the complex interaction between the charged spacecraft and the ambient plasma (Odelstad et al., 2017; Johansson et al., 2020, 2021). The couplings between probe and spacecraft, and probe and plasma, can both differ between the two probes, with each probe picking up a different fraction of the spacecraft potential and having a different floating potential w.r.t. the plasma. We make a crude but effective correction for such effects by making a linear fit of the potential V_1 of LAP1 to V_2 of LAP2, and then using the resulting fitting parameters to shift and rescale V_2 to match V_1 as closely as possible over some suitable time interval (see below). The remaining difference between V_1 and the scaled and shifted V_2 is then divided by the probe separation distance (5.00 m) to obtain an estimate of the electric field component between the probes.

LAP operational modes are organized in 32 s long sequences with a brief gap (~ 1 s) at the end of each sequence (Odelstad et al., 2020). We use these sequences as the time intervals over which to apply the correction described above. When direct measurements of the spacecraft potential are required, e.g. when calculating the ion distribution moments from ICA differential fluxes (see below), the average of V_1 and the scaled and shifted V_2 will be used, with an additional empirical correction (equation (1) of Johansson et al., 2021).

2.2 The Ion Composition Analyzer (RPC-ICA)

ICA (Nilsson et al., 2007) is an electrostatic analyzer of a spherical top-hat configuration measuring three-dimensional distributions of positive ions in the energy range 5 eV/q to 40 keV/q over a field of view (FOV) of $90^\circ \times 360^\circ$, combined with a magnetic momentum filter that resolves the major ion species such as protons, helium and water group ions. The 360° azimuthal FOV is distributed over 16 anodes, each with a width of 22.5° . The aperture is $360^\circ \times 5^\circ$; the 90° elevation FOV is achieved by varying the voltage across two electrostatic deflector plates, effectively scanning 16 different angles in the range $\pm 45^\circ$. The time required for a full scan in elevation and energy is 192 s, however a special high time resolution mode has been implemented (Stenberg Wieser et al., 2017) in which the elevation angle is kept fixed at close to 0° and the energy range is truncated to 5-95 eV/q, reducing the integration time to 4 s. Due to the highly variable and rapidly changing cometary ion environment, the ion data in this work comes exclusively from this high time resolution mode, which was only run intermittently during the mission. It should be noted that the resulting ion observations are effectively two-dimensional, with a FOV of $5^\circ \times 360^\circ$ in the zero-elevation plane. Under nominal spacecraft pointing conditions, this plane includes both the comet and the Sun, but ion fluxes outside of this plane cannot be observed.

2.3 The Mutual Impedance probe (RPC-MIP)

MIP (Trotignon et al., 2007) uses the mutual impedance spectra of two pairs of dipole antennas to obtain the plasma density from characteristic signatures that appear in these spectra at or near the plasma frequency. Measurements are obtained with a cadence $\gtrsim 2.5$ s. A MIP/LAP cross-calibrated dataset has been produced, where an empirical relation be-

tween the LAP1 floating potential (used here as a proxy for $V_{S/C}$) and MIP plasma densities is established by fitting simple analytical models over overlapping time windows, and using this to recalibrate the LAP voltage data to density values (Breuillard et al., 2019). This dataset thus has the same time resolution as the LAP data, up to ~ 60 Hz, and is more suitable for detailed wave analysis in the frequency range of interest here.

2.4 The Fluxgate Magnetometer (RPC-MAG)

MAG (Glassmeier, Richter, et al., 2007) is a triaxial fluxgate magnetometer mounted 1.5 m out from the spacecraft main body on the same boom as LAP2. It samples three orthogonal components of the magnetic field at a resolution of 31 pT in a range of $\pm 16 \mu\text{T}$ at a frequency of 20 Hz. The magnetic field measurements are subject to disturbances from the spacecraft and the other instruments onboard; the most prominent of these, the influence from the reaction wheels, lies in the frequency band 2–10 Hz, i.e. exactly in the lower hybrid frequency range of interest here. We do not use the MAG data for investigating the waves in this work; we use it to compute the lower hybrid frequency, and to give some background information and context on the plasma environment. For this, we use data downsampled to 1 Hz, by forward and reverse filtering the 20 Hz data with a Butterworth IIR lowpass filter and then interpolating to sample times 1 s apart (same procedure as in Goetz, Koenders, Hansen, et al., 2016).

3 Results

3.1 Primary example

Figure 1 shows a selection of data (about 20 min) from 25 October 2015, when LAP electric field measurements and ICA high time resolution measurements were simultaneously available. The cometocentric distance was 350 km and the heliocentric distance was 1.5 AU. (Data from this same day were also examined in Karlsson et al. (2017).) In Figure 1a we show plasma density data. The density here is often fairly stable around 100 cm^{-3} , but intermittently increases several-fold, up to as much as 500 cm^{-3} , typically on time-scales of one to a few minutes.

Figure 1b shows magnetic field data. The magnetic field strength is highly variable, most often in the range 20–50 nT, but sometimes dropping below 20 nT down to about 10 nT. There is also the odd peak reaching up to ~ 70 nT. Magnetic field enhancements occur on time-scales of typically a few minutes. They are often asymmetric, with much higher rise times than decay times, and may be related to similar structures observed near the diamagnetic cavity (e.g. Goetz, Koenders, Hansen, et al., 2016; Henri et al., 2017; Hajra et al., 2018; Odelstad et al., 2020) and/or steepened fast magnetosonic waves discussed by Ostaszewski et al. (2021). Also shown in Figure 1b are a number of angular quantities (to be read off the right-hand y-axis): cone angle θ_B (red line) and clock angle ϕ_B (green line) of the magnetic field (to be defined below), the angle α_{EB} (blue line) between \mathbf{B} and the probe separation vector \mathbf{d} (c.f. Section 2.1) corresponding to the direction of the observed electric field component, and finally the angle α_{rB} (yellow line) between the outward radial direction from the comet and the magnetic field. α_{rB} is most often very close to 90° , thus the highly draped magnetic field is perpendicular to the radial direction from the comet. α_{EB} is most often close to 90° , so the electric field component that we observe is close to perpendicular to the ambient magnetic field (as expected close to a diamagnetic cavity). Rosetta magnetic field data are often presented in a Comet-centered Solar-Equatorial (CSEQ) coordinate system, in which the +X axis points towards the Sun, the +Z axis is the component of the Sun’s north pole of date orthogonal to the +X axis, and the +Y axis completes the right-handed reference frame. We define the cone angle of a vector (e.g. position, magnetic field) as the angle of elevation from the YZ plane; it falls in the interval $[-90^\circ, 90^\circ]$ and is positive for sunward and negative for anti-sunward directions, respectively. θ_B in Figure 1b is most

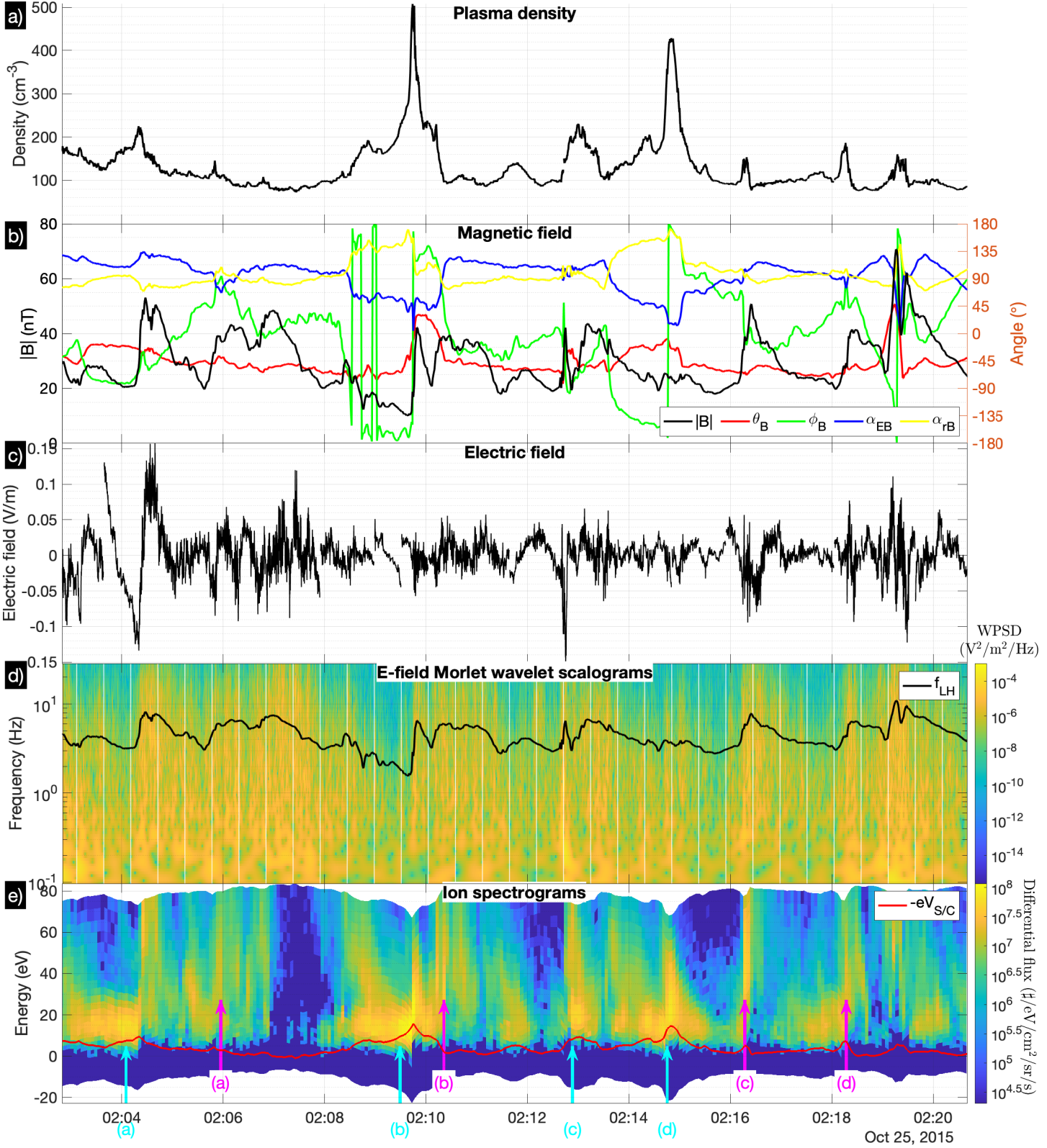


Figure 1. Overview of plasma data from selected time interval. **a)** Plasma density. **b)** Magnetic field magnitude (black line, left-hand y-axis) and orientation (right-hand y-axis): cone and clock angles (θ_B and ϕ_B , red and green lines), angle α_{EB} to the measured electric field component (blue line) and the angle α_{rB} to the outward radial direction from the comet (yellow line). **c)** LAP electric field measurements. **d)** Wavelet scalograms of the electric field, and lower hybrid frequency f_{LH} (black line). **e)** ICA high time resolution ion spectrograms. Magenta and cyan arrows highlight spectrograms selected for more detailed analysis in Figures 2 and 3, respectively.

often close to -45° , indicating a predominantly anti-sunward direction of the magnetic field. The clock angle is the azimuth angle in the YZ plane, in the direction from Y towards Z, taking values in the range $[-180^\circ, 180^\circ]$ (same as e.g. Masunaga et al., 2019; Bergman et al., 2021). For the epoch shown in Figure 1b, the clock angle of the spacecraft position vector was close to zero ($|\phi_{\mathbf{r}_{\text{sc}}}| \lesssim 2.5^\circ$). With both the Sun and the comet in the ICA aperture plane, this means that the Z axis in the CSEQ frame was close to aligned with the ICA symmetry axis, and the clock angle of a vector thus a good proxy for the elevation angle above the ICA aperture plane.

The electric field from LAP is shown in Figure 1c. Unlike in Karlsson et al. (2017) and André et al. (2017), we have not performed any high-pass filtering of these data. The linear fit and rescaling of V_2 to V_1 employed in the electric field computations (c.f. Section 2.1), being applied separately to each 32-s sequence of uniform sampling, introduces clear artificial discontinuities at the transitions between some such segments; these lack physical significance. The electric field data exhibit significant dynamics on multiple time scales. Large-scale features appear on longer time scales, several seconds up to a few minutes, exhibiting both quasi-harmonic (e.g. around 02:06–02:07) and an-harmonic (e.g. around 02:03–02:05) low-frequency oscillatory behavior, as well as more short-lived pulse-like events (e.g. around 02:13). It is not clear to what extent any or all of these features actually represent electric fields, or if they are spurious features caused by e.g. changes in the probe-plasma coupling of the individual probes. The focus of this study is instead on the shorter-timescale oscillations that appear throughout the selected time interval. These are likely real electric fields, and will be interpreted as such throughout this paper. Wavelet scalograms were computed of the electric field data (separately over each 32-s sequence of uniform sampling, c.f. Section 2.1) and these are shown in Figure 1d, together with the H_2O^+ lower hybrid frequency f_{LH} (black line) computed from the magnetic field data. We may identify two quite distinct frequency ranges: one of persistent low-frequency broadband activity below ~ 0.5 –1 Hz and another with more variable amplitudes at frequencies above that. The latter corresponds broadly to the lower-hybrid frequency range and represents the shorter-timescale oscillations that we interpret as electric field fluctuations. Thus the high-pass filtering at around 1 Hz and 0.5 Hz of Karlsson et al. (2017) and André et al. (2017), respectively, appear to have fairly accurately isolated the electric field oscillations from more ambiguous features in the data.

The varying power in the lower hybrid frequency range may at least at times be characterized as localized bursts or wave packets of large electric field amplitude (0.01–0.05 mV/m), typically persisting for a few seconds, up to at most about 15–20 s (e.g. around 02:05, 02:16:30 and 02:19). It is the perceived correlation between such wave packets and pronounced plasma density gradients that forms the basis for attributing such wave activity in the inner coma to the lower-hybrid drift instability (Karlsson et al., 2017; André et al., 2017). While data presented for selected time intervals in Karlsson et al. (2017) were fairly convincing in this regard, the data we show in Figures 1c–d are less so. Some of the steepest density gradients observed do not coincide with very strong wave activity (e.g. around 02:09 and 02:15), and substantial wave activity occur also in the absence of strong gradients in plasma density as gauged by the combined LAP/MIP data in Figure 1a (e.g. between about 02:05 and 02:08). The lowest wave activity appears to occur at times when the magnetic field strength becomes unusually low, $\lesssim 20$ nT (e.g. around 02:09–02:10 and 02:15–02:16). A comprehensive statistical correlation study between lower hybrid wave activity and density gradients, magnetic field strengths, and possibly other parameters as well, is beyond our scope here, but might be a pertinent topic for future work. Here we settle on the proposition that additional plasma instabilities, beyond the lower hybrid drift instability, should be investigated as possible wave generation mechanisms in this plasma environment.

Several previous works have shown the existence of multiple populations of cometary ions in the inner coma of 67P, distinguished by differences in energy and/or flow direc-

tion (e.g. Berčič et al., 2018; Nilsson et al., 2020; Bergman et al., 2021). Consequently, we choose in this work to investigate the possible role of ion streaming instabilities for generating the observed lower hybrid waves. For this purpose, high time resolution ion spectrograms from ICA are shown in Figure 1e. The ion energies have here been shifted by the spacecraft potential obtained by LAP (c.f. Section 2.1), but the latter is also plotted on top of the spectrograms (red line), with reversed sign and scaled by the elementary charge q_e to facilitate comparison with the (singly charged) ion energies. Measurements of ions with energies $\lesssim 2q_e|V_{S/C}|$ (prior to acceleration by the spacecraft potential) may be heavily distorted by the electrostatic field of the charged spacecraft, but ions with energies higher than that should not be significantly affected, according to particle tracing simulations by Bergman et al. (2020a). The ion data here are clearly quite erratic, with substantial variations of flux and energy on very short time-scales. However, a band of low-energy ions with energies $\lesssim 30$ eV can at times be discerned (perhaps most clearly around 02:04 and 02:10 in Figure 1e). Ions with higher energies are also intermittently observed, sometimes in addition to the low-energy ion band, sometimes without it. At times (e.g. around 02:07) no ions are observed at all.

In Figure 2 we present in more detail selected examples of individual ICA ion spectrograms, indicated with magenta arrows in Figure 1. These have been chosen to showcase typical characteristics of the higher-energy ions. In the first column of Figure 2 (panels a–d) we show two-dimensional energy-angle polar histograms of the ion fluxes. The bin colors denote observed differential flux of ions in each energy-angle bin during the 4-s integration time of the instrument. The radial location of each bin corresponds to the energy of collected ions, corrected for the spacecraft potential (the radial axis has units of eV). Azimuth bin locations correspond to the arrival direction of the ions into the instrument. The polar angle in the plot corresponds to the azimuth angle in the instrument reference frame (Nilsson et al., 2007) and red text labels indicate the standard ICA sector numbering. Sectors 1 and 13 have very low sensitivity, rendering the instrument effectively blind in these directions, and Sector 0 is subject to cross-talk and noise, picking up signal from the other sectors (Berčič, 2017). These sectors have therefore been grayed out in Figures 2a–d. Also, Sector 2 is somewhat more sensitive than the other sectors and need to be considered with care. For the near-terminator orbit of the spacecraft at this time, the directions of the Sun and comet (red arrows) are in sector 10 and between sectors 4 and 5, respectively. The average magnetic field vector projected onto the ICA aperture plane is along the view direction of sector 1 in all four cases. The average magnetic field magnitude $|\mathbf{B}|$ and elevation angle $\theta_{\mathbf{B}}$ above the ICA aperture plane are printed in the top left of the respective panels; they are between about 30–40 nT and around -35° , respectively, in all four cases. The average spacecraft potentials during the respective intervals are similarly printed at the bottom left of each panel. They are about -3 V to -2 V in the first two cases (a and b) and -7 V to -5 V in the latter two cases (c and d). All four examples shown in Figure 2 exhibit large fluxes in sectors 11 and 12. These sectors point in the direction opposite to the comet, so ion fluxes observed here represent inward radial flow, towards the comet nucleus. They are also highly oblique, almost perpendicular to the magnetic field component in the sensor plane. Besides that, fluxes are generally very weak, with the possible exception being some more or less radially outflowing (anti-cometward) flows in 2 a and d; we will return to this point in connection with Figure 3 below, where clearer examples of this will be shown.

In the second column of Figure 2 (panels e–h) we show the differential flux in each energy bin for sectors 11 and 12. Ion fluxes typically peak at energies around 40 eV, with broad spreads in the range from ~ 10 eV up to at least 80 eV. We have computed moments of these distributions (c.f. Nilsson et al., 2020, Appendix A); the results are printed in the respective panels of Figure 2 with text colors corresponding to the respective histogram colors. All four examples shown have bulk drift velocities $\langle v_i \rangle$ to 20 km/s and thermal velocities (in the direction parallel to the flow) $\langle v_{ti} \rangle$ around 3–4 km/s, corresponding to temperatures $\langle T_i \rangle$ in the range 2–4 eV. Summing the two sectors,

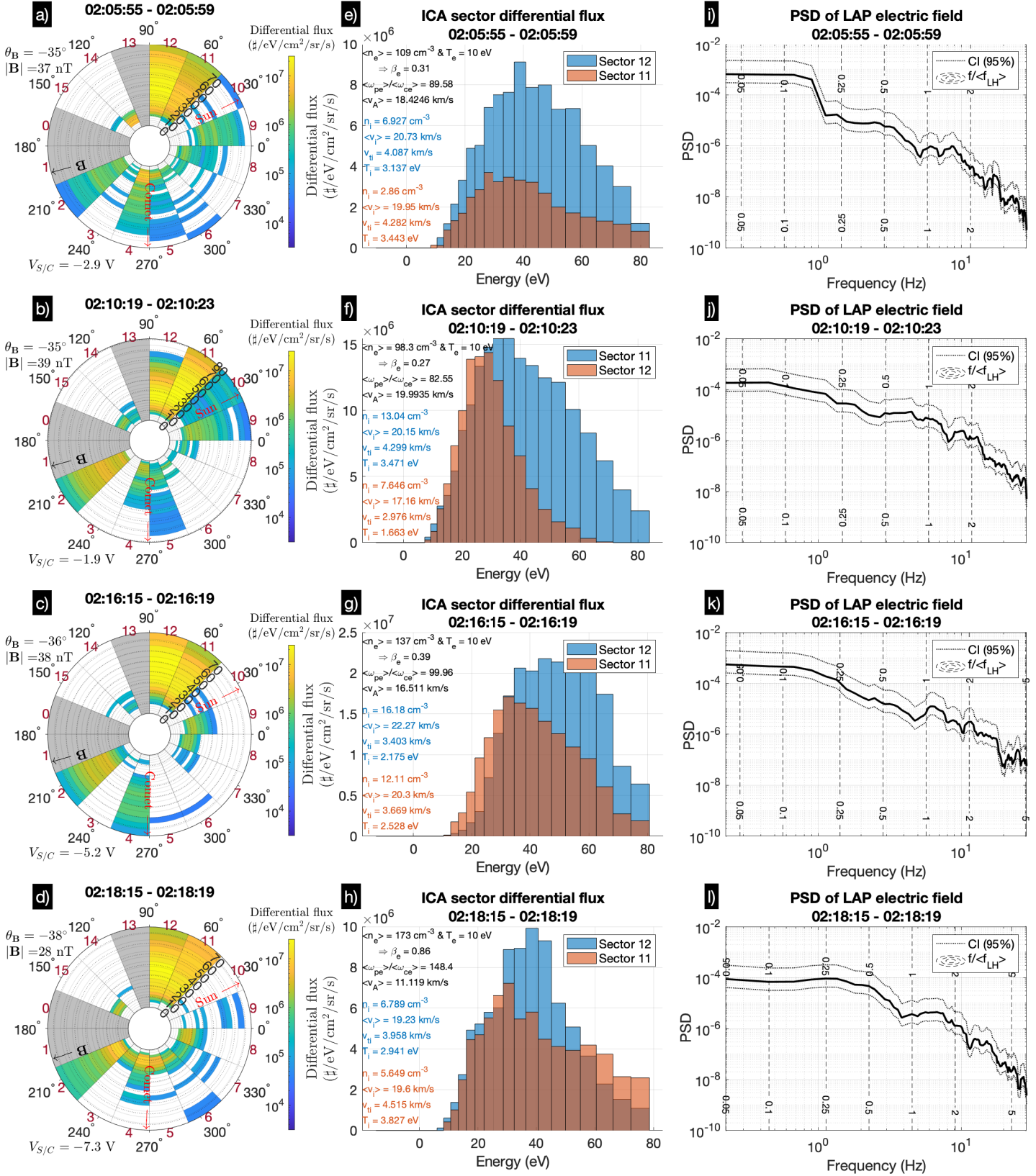


Figure 2. Examples of inward-streaming accelerated ions, corresponding to ICA spectrograms highlighted with magenta arrows in Figure 1. **a – d)** Energy-angle polar histograms of ion fluxes. **e – h)** Differential flux in each energy bin for sectors 11 and 12. **i – l)** Concurrent power spectral densities of LAP electric field data.

densities are in the range $10\text{--}30\text{ cm}^{-3}$, ranging from a few up to almost 30 percent of the total plasma density. The black text at the top left gives average plasma parameters for each sample time interval. n_e and β_e are the plasma density and electron plasma beta, calculated assuming an electron temperature T_e of 10 eV. (There are no Langmuir probe sweeps when LAP is measuring electric fields, so there are no local T_e measurements available. Hence a typical $T_e \sim 10$ eV is used.) β_e is between 0.3 and 0.9 for these cases. ω_{pe}/ω_{ce} is the ratio of electron plasma and cyclotron frequencies. It is typically on the order of 10^2 , thus the plasma is clearly overdense. v_A is the Alfvén velocity. We may note that v_A is often very close to or slightly below the ion bulk drift velocity.

In the third column of Figure 2 (panels i–l) we show power spectral densities of LAP electric field data, computed over each 4-s ICA sampling interval using Thomson’s multitaper method (Thomson, 1982). Dashed vertical contour lines indicate fractions of the lower hybrid frequency (calculated from MAG data) and dotted lines indicate 95% confidence intervals (computed using the inverse chi-square distribution, e.g. Kay, 1988). A clear spectral peak just above the lower hybrid frequency can be observed in Figure 2 i. In the other plots, such features are not as clearly present, although we may note if not significant peaks at least clear plateaus in the spectra near or around the lower hybrid frequency.

In Figure 3 we show a different selection of example ICA ion spectrograms, indicated with cyan arrows in Figure 1. These have been chosen to illustrate typical behaviour of the low-energy ion band, as well as some more complicated cases. Generally, the magnetic field strengths are lower here than for the examples in Figure 3, resulting in larger β_e and lower Alfvén speed. Total plasma densities are also typically somewhat higher. In panels a and d, the ion flux is entirely dominated by low-energy ($\lesssim 20$ eV) ions in sectors 5–8. These ions thus flow anti-cometward (sector 5) and some of them also have clear anti-sunward velocity components (sectors 6–8). They are also close to perpendicular to the magnetic field component in the sensor plane. In panels b and e we show the differential flux vs. energy for sectors 5 and 8, with computed moments printed in the plot as before. Most of the differential flux is in the range 0–30 eV, peaking around 15–20 eV. The moment calculations here indicate densities in the range $5\text{--}10\text{ cm}^{-3}$ for the individual sectors; combined this accounts for less than 10% of the total densities $\langle n_e \rangle$ at these times. The bulk drift velocities are 11–13 km/s for these examples, and the thermal velocities are around 2 km/s, corresponding to temperatures of around 1 eV.

Panel g shows an example of a more mixed case, where the radially outflowing band of low-energy ions (sectors 5–6) is observed simultaneously with higher-energy ions. The latter are confined to sectors 11 and 9, indicating cometward flux with an anti-sunward (especially for sector 9) component. There are no known measurement issues with sector 10, so the angular separation appears to indicate a clearly bi-modal angular distribution of the accelerated ions here, although we make no claims about the universality of this feature in the data. In panel h, we show the differential flux vs. energy for sectors 6 and 9. Clearly, these represent two populations distinct in energy, as well as flow direction. We may also note that the flow in sector 9 appears to be close to field-parallel, while sector 11 has a more of a cross-field component. Finally in panel j we show an example with maximum flux in sector 8, and smaller (but still substantial) fluxes in sectors 5–7. Differential flux vs. energy is shown for sectors 7 and 8 in panel k. Here, it is not as clear that there are two distinct ion populations, well-separated in energy and flow direction. It is possible that we are looking at a single population with broad spread in both energy and flow direction. However, it is also possible that there are in fact two distinct populations here, just as in panel h, only their angles and energies happen to be closer, partially overlapping each other. The spread in arrival angle (and to some extent, energy) of the low energy ions toward the anti-sunward direction sometimes makes it difficult to determine if large flows in sectors 8–9 are of separate origin, or if they are a high-

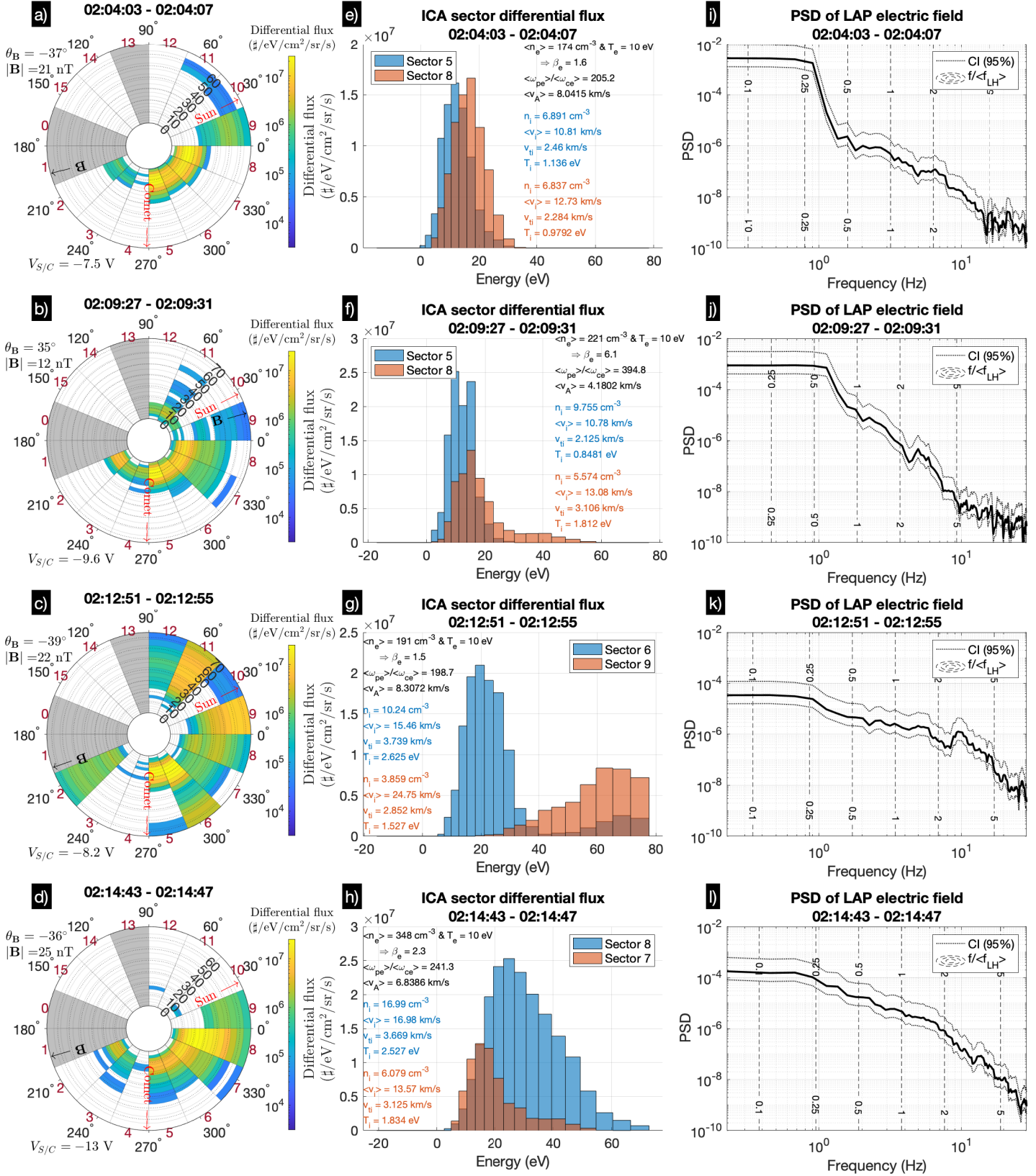


Figure 3. Examples of outward-flowing cold ions, corresponding to ICA spectrograms highlighted with cyan arrows in Figure 1. **a – d)** Energy-angle polar histograms of ion fluxes. **e – h)** Differential flux in each energy bin for selected sectors. **i – l)** Concurrent power spectral densities of LAP electric field data.

energy tail of the low-energy population. Again, the accelerated ion flux appears to have at least some component of the motion across the magnetic field.

Finally, the right-most column in Figure 3 shows the power spectral densities of LAP electric field data for the selected times. We tentatively identify peaks in the spectra in panels f and i at frequencies somewhat above twice the lower hybrid frequency, although the significance of these may not be entirely clear. We may observe if not plateaus so at least an increase in spectral slope in the vicinity of $2f_{\text{LH}}$.

3.2 Supplementary example

The data shown and described so far all come from a brief (20 min) interval on 25 October 2015, when LAP electric field measurements and ICA high time resolution measurements were simultaneously available. LAP double-probe floating potential measurements were carried out intermittently from May 2015 until end of mission (30 September 2016). Observations by ICA in high time resolution mode are available intermittently from late May 2015 to late August 2016. We make no attempt at a comprehensive survey of these data here. To show that the selected data are not a singular aberration, we show just one more example: Figure 4 shows a multi-instrument overview of data for a time interval on 15 November 2015, 17:03–17:23 UTC. (Also data from this day have previously been examined in Karlsson et al. (2017).) The figure layout here is the same as in Figure 1. The heliocentric distance was here 1.67 AU and the cometocentric distance was 149 km. The plasma density in Figure 4a is mostly in the same range as for the previous event, ranging from around 100 cm^{-3} up to a few hundred cm^{-3} . However, the data here appear less structured and more dynamic, with a lot more variability on shorter timescales as compared to Figure 1a. The magnetic field in Figure 1b is somewhat higher than before, about 30–50 nT with values above 30 nT being much more prevalent than in the previous case. Also here the data are less structured with more dynamics on shorter time scales. The previously dominating asymmetric magnetic field enhancements on timescales of minutes appear to be largely absent here. The angular quantities in Figure 4b are largely similar to the ones in Figure 1b, indicating an overall similar geometry of the magnetic field. The electric field data in Figures 4c–d show high levels of wave activity in the lower hybrid frequency range throughout this interval. Amplitudes are often similar to the previous event (0.01–0.05 mV/m), but any characterization in terms of localized bursts or wave packets seems less clear, or at least the wave packets are now shorter and more frequent, giving a less structured appearance to the data. Finally, in Figure 4e, the ICA ion spectrograms are again clearly quite erratic, with substantial variations of flux and energy on very short time-scales. However, the band of low-energy ions with energies ($\lesssim 20 \text{ eV}$ in this case) can still be discerned. Again, ions with higher energies are also intermittently observed, and there are times (e.g. around 17:06) when little or no ions are observed at all.

In Figure 5 we again show a selection of example ICA ion spectrograms, indicated with magenta arrows in Figure 4. The energy-angle polar histograms in the first column (panels a,d,g and j) exhibit similar features to the ones in Figures 2 and 3: Higher-energy ions are often observed in sectors 11–12, i.e. flowing back towards the comet nucleus. Again, these accelerated ion flows appear to have a significant cross-field component. The low-energy band of ions, when observed, typically exhibit the largest fluxes in directions radially outward from the comet (e.g. panel a), sometimes with an angular spread towards the anti-sunward direction (e.g. in panel d). Moments of the accelerated ions (second column, panels b,e,h and k) indicate flow speeds of 15–20 km/s, very close the Alfvén velocity that ends up in that same range, ion thermal velocities in the range 2–4 eV, and densities up to about 30 cm^{-3} (panels b and h), corresponding to up to 20% of the total plasma density. β_e is between 0.2 and 0.8 for these cases, basically the same as for the previous event, and the plasma is still overdense, with $\omega_{\text{pe}}/\omega_{\text{ce}} \sim 10^2$. The power spectral densities of LAP electric field data for the selected times, shown in the right-

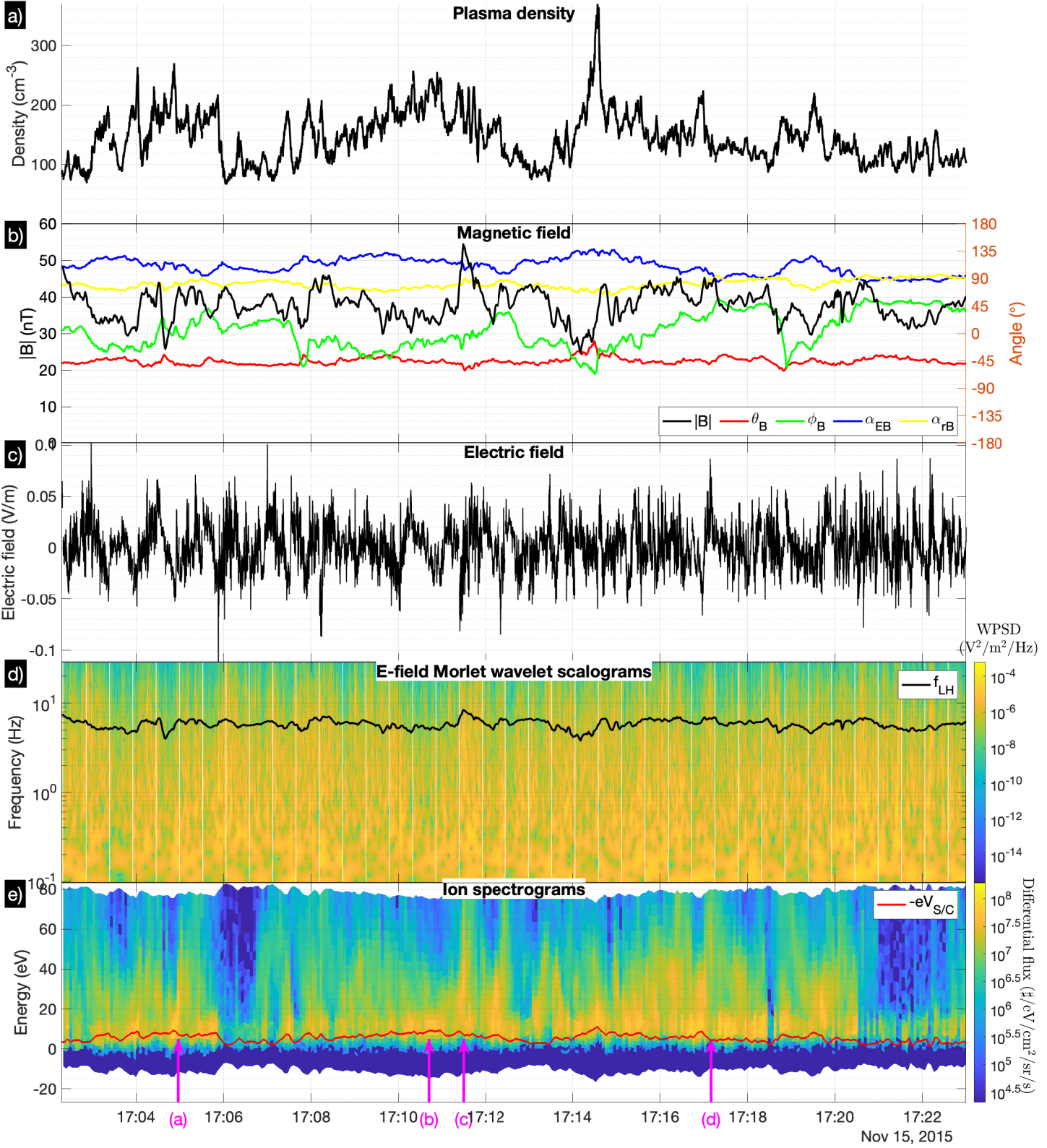


Figure 4. Overview of plasma data from selected time interval. **a)** Plasma density. **b)** Magnetic field magnitude (black line, left-hand y-axis) and orientation (right-hand y-axis): cone and clock angles (θ_B and ϕ_B , red and green lines), angle α_{EB} to the measured electric field component (blue line) and the angle α_{rB} to the outward radial direction from the comet (yellow line). **c)** LAP electric field measurements. **d)** Wavelet scalograms of the electric field, and lower hybrid frequency f_{LH} (black line). **e)** ICA high time resolution ion spectrograms. Magenta arrows highlight spectrograms selected for more detailed analysis in Figure 5.

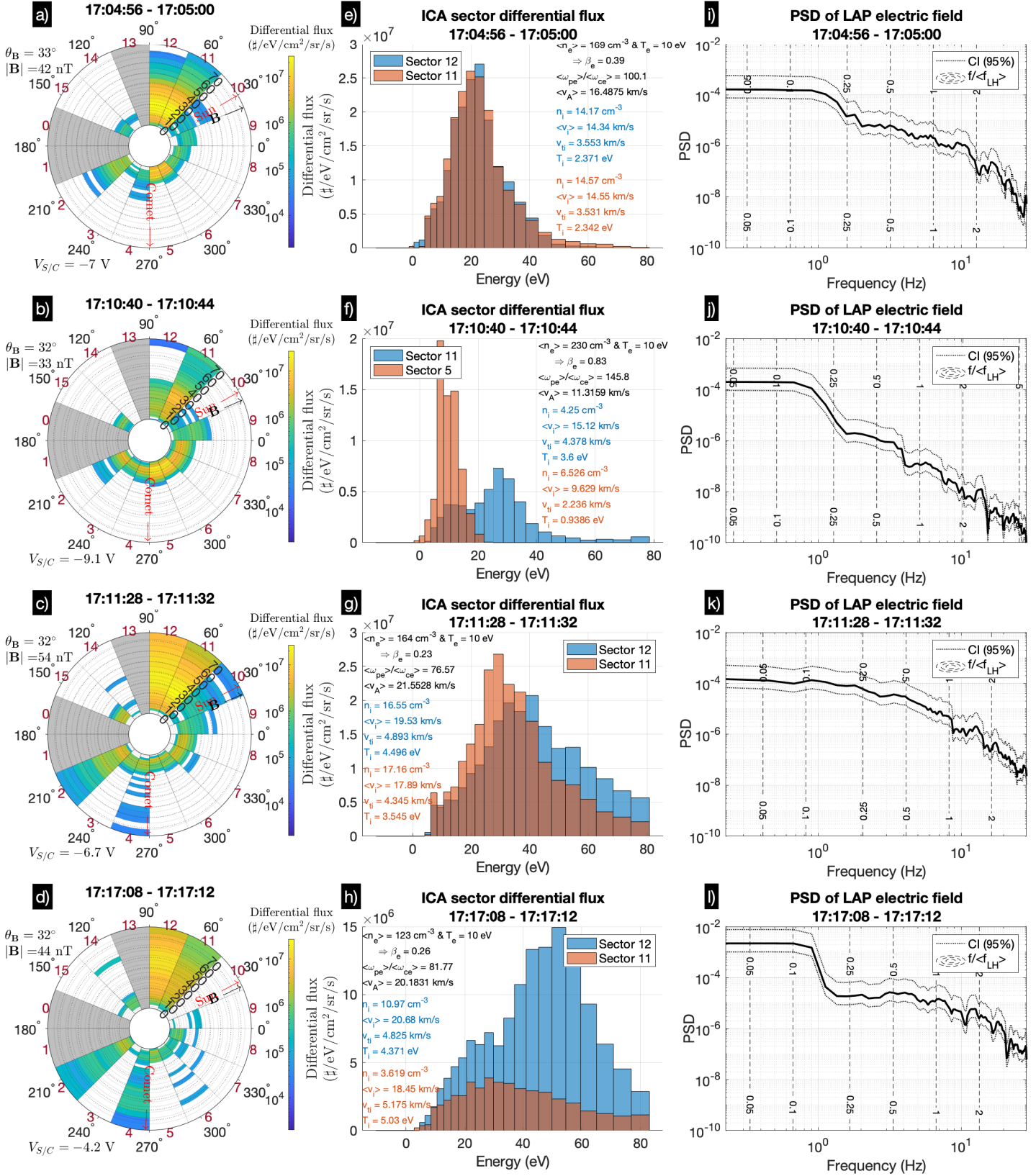


Figure 5. Example ICA ion fluxes, corresponding to ICA spectrograms highlighted with magenta arrows in Figure 4. **a – d)** Energy-angle polar histograms of ion fluxes. **e – h)** Differential flux in each energy bin for selected sectors. **i – l)** Concurrent power spectral densities of LAP electric field data.

most column in Figure 5 (panels c,f,i and l), indicate similar power levels of fluctuations in the lower hybrid frequency range as for the previous event, but there does not appear to any clear spectral peaks in any of these examples. We conclude that most of the features described here correspond well to the first event, both qualitatively and quantitatively, and are therefore likely recurring characteristics of the plasma environment in the inner coma of 67P during the high-activity phase of the mission from which these examples were taken.

4 Discussion

Several authors (e.g. Huba & Wu, 1976) have pointed out the effects of gradients in the magnetic field on the lower-hybrid drift instability. These are complicated, and can be either stabilizing or destabilizing depending on the specific physical conditions. This generally requires a full electromagnetic treatment, including inhomogeneities, which is beyond the scope of this paper. Instead, we focus here on examining the ion-ion cross-field instability driven by counter-streaming ions across the magnetic field.

4.1 Ion flows

In the early low- to intermediate-activity period of the Rosetta mission (September 2014 to April 2015), two distinct cometary ion populations were typically observed by ICA (Nilsson et al., 2015; Behar et al., 2016; Berčič et al., 2018), separated by their energy range and flow direction: (1) ions with an energy $\lesssim 50$ eV coming from between the Sun and comet direction, identified as locally produced cometary ions expanding outward from the comet, and (2) more energetic ions with an arrival angle centered on the Sun direction, identified as cometary ions picked up further out by the convective electric field of the upstream solar wind, and accelerated back towards the comet. Berčič et al. (2018) reported mean speeds and densities of the low energy ions of 6 km/s and $10\text{--}20\text{ cm}^{-3}$ during a period between 26 December, 2014 and 23 January, 2015; for the pick-up ions they found ~ 30 km/s and $0.1\text{--}0.4\text{ cm}^{-3}$, respectively, during the same period. The flow direction of (1) was radially outward in the terminator plane, with an additional anti-sunward component symmetrically about the comet-Sun line (c.f. Fig. 4 of Berčič et al., 2018). The pick-up ions (2) had a similar anti-sunward velocity component, but the flow in the terminator plane was consistently along the direction of the (varying) upstream solar wind electric field direction, as gauged from the bulk flow of solar wind protons and alpha particles (often heavily deflected from the anti-sunward direction).

The combination of terminal-plane radial expansion and out-of-plane anti-sunward velocity of the lower-energy cometary ions persisted also during the subsequent period of higher comet activity (Nilsson et al., 2020), however the behaviour of the pick-up ions changed. From late April 2015 to mid-December 2015, a "solar wind cavity" formed in the inner coma, as the solar wind ions (protons, alphas) were entirely deflected away (Behar et al., 2017). Inside this cavity, the pick-up ions exhibited a clear deflection in the direction *opposite* to the solar wind electric field (as gauged from the magnetic field direction, c.f. Edberg et al., 2019), just like the solar wind did at lower activity levels. Thus, these pick-up ions had effectively taken over the role of the solar wind for the momentum transfer into the inner coma (Williamson et al., 2020). The low energy ions maintained typical flow speeds of 5–10 km/s throughout the mission, while the pick-up ions generally had flow speeds $\gtrsim 20$ km/s (Nilsson et al., 2020, Figs. 1–2). Average densities were generally $10\text{--}100\text{ cm}^{-3}$ and $\lesssim 10\text{ cm}^{-3}$, respectively (Nilsson et al., 2020, Fig. 3).

These results were obtained from full 192-s scans in elevation and energy, and for the most part also averaged over 24 h. In reality, and as shown in this and other work (e.g. Stenberg Wieser et al., 2017), there was a significant amount of variation and dynamics on much shorter time-scales, even shorter than the 192-s integration time. Hence,

use of the high time resolution mode (c.f. Section 2.2) is required. Here, the energy range is reduced to 5–95 eV/q and the FOV is restricted to $5^\circ \times 360^\circ$ in the zero-elevation plane, which normally contains both the comet and the Sun. Ions with velocity vectors well out of this plane will thus not be observed. From the flow patterns outlined above, the low energy ions (1) would nominally fall into this plane, since their average motion predominantly has anti-cometward and anti-sunward components. However, the detailed distributions were often shifted slightly in elevation angle as well (Berčič et al., 2018; Nilsson et al., 2020), frequently falling just outside of the zero-elevation plane. It is not clear whether or not this was an effect of the spacecraft potential affecting the ion trajectories. The pick-up ions (2), having a large terminator-plane velocity component along/opposite to the varying upstream solar wind electric field, should presumably be observed only intermittently in the high time resolution mode, requiring favourable upstream solar wind conditions.

The total density of cometary ions observed by ICA, even in full 3D scans, is typically much lower than that observed by LAP and MIP, often by one or two orders of magnitude (Nilsson et al., 2020). Thus, ICA clearly does not capture all of the low-energy ions of the cometary plasma. Cometary ions are born with the same velocity as their parent neutral molecules, which flow radially outward at $\lesssim 1$ km/s. Subsequent acceleration is primarily in the outward radial direction due to the ambipolar electric field, at least inside the diamagnetic cavity. Outside of this cavity, their trajectories may be influenced by the magnetic field. However, an outward radial ambipolar electric field should still persist, also outside the diamagnetic cavity, since quasi-neutrality has to hold on length scales on the order of the Debye length, which at $\lesssim 1$ m is orders of magnitude smaller than the gyro-radii of the cometary ions. This radial field is clearly seen in Particle-In-Cell (PIC) simulations by Deca et al. (2019). We thus presume that the bulk of cometary ions making up the difference between the densities observed by ICA and LAP/MIP are low energy ions moving predominantly radially outward. The anti-cometward low-energy ion population intermittently observed in ICA spectrograms in Section 3 thus likely correspond to some small fraction of this bulk population of cometary ions, perhaps a high-energy tail. The reason for their only intermittent appearance in ICA high time resolution spectrograms may be, at least in part, due to them acquiring a transverse velocity component, owing to the Lorentz force in the ambient magnetic field, which could divert them out of the ICA aperture plane. This hypothesis may claim some support from the apparent tendency of this low-energy band of ions in the ICA spectrograms to appear in coincidence with unusually low magnetic field strengths ($|\mathbf{B}| \lesssim 20$ nT).

The spacecraft potential may also have a significant impact on these low-energy ions, distorting the directional information and effectively changing the instrument FOV in this energy range. Bergman et al. (2021) used PIC simulation results to attempt to correct for these effects in ICA high time resolution data. Their study was limited to the ion flows in and around the diamagnetic cavity, i.e. a plasma environment that may differ from the examples shown here. For a spacecraft potential of -13 V and a Debye length of 0.66 m, the correction was usually around 1–2 sectors ($22.5^\circ - -45^\circ$) for the lowest ion energies, thus not so much that it would dramatically change the results we present here. The Debye length here is also most likely larger (~ 2 m for $n_e \sim 100$ cm $^{-3}$ and $T_e \sim 10$ eV), which should generally lead to less distortion of the FOV (Bergman et al., 2020b). Interestingly, Bergman et al. (2021) found similar “burst” and “band” features in the ion data as we present here, but with the bursts flowing radially outward from the nucleus (with an antisunward component) while the band was predominantly streaming back towards the comet. Thus, quite the opposite configuration to what we observe in this study, further away from the diamagnetic cavity. The amount of ions flowing radially outward was surprisingly small, indicating again that the bulk of cometary ions was not observed by ICA, likely due to FOV effects. In fact, PIC simulations showed that strictly radially outflowing ions would be deflected in elevation, indeed ending up outside the instrument FOV for these 2D measurements, at least for ion energies as low

as 5–10 eV and a spacecraft potential as negative as -20 V (Bergman et al., 2021, Fig. 9).

We propose that the predominantly cometward-flowing ions sometimes observed in Section 3 are the pick-up ions created further out and accelerated back towards the comet. As described above, at this stage of the mission they are typically deflected away from the anti-sunward direction in the direction opposite to the solar wind electric field, which is perpendicular to the magnetic field in the terminator plane. This would thus produce a cross-field drift of these ions. (A graphical illustration of this configuration is shown and further elaborated on below.) Depending on the direction of the solar wind electric field in the terminator plane, this could have a component of the motion either towards or away from the comet. In the former case, they could be observed as the cometward-flowing ions in Section 3, at times when the solar wind electric field is close enough to the instrument aperture plane to allow them to be detected at all in the high time resolution mode. In the latter case, they would likely be intermixed with the out-flowing cometary ions in Section 3, again requiring favourable solar wind electric field direction to enter the instrument close enough to the aperture plane.

An illustration of the electric and magnetic fields, and the resulting ion flows, is shown in Figure 6. The coordinate system here has the x-axis pointing towards the Sun and the z-axis aligned with the ICA symmetry axis. For the time interval shown in Figure 1 the location and attitude of the spacecraft combine so as to very nearly align the ICA symmetry axis with the Z axis in the CSEQ coordinate system. The coordinate system in Figure 6 may therefore just as well be the CSEQ system in this case. We have put the ICA sector plane precisely in the terminator plane in Figure 6; for the time interval shown in Figure 1 the spacecraft is actually located about 30° out of this plane, in the direction towards the Sun. This is why the comet and Sun directions in Figure 1 are not exactly 90° apart in ICA’s FOV, as they would be if exactly in the terminator plane. This should not affect the qualitative reasoning developed here. The blue arrow indicates the total magnetic field vector \mathbf{B} and the green arrow its projection onto the terminator plane \mathbf{B}_p . The cyan arrow indicates the presumed direction of the upstream solar wind electric field \mathbf{E}_{SW} , as estimated from the cross-product $\hat{\mathbf{x}} \times \mathbf{B}_p$ (Edberg et al., 2019). The ambipolar electric field (\mathbf{E}_{amb} , black arrow) is directed radially outward from the comet nucleus and there is also an anti-sunward polarization electric field (\mathbf{E}_{pol} , red arrow, c.f. Nilsson et al., 2018). Dashed lines are used to indicate projections of various vectors onto different planes, to give a better 3D perspective and sense of depth in the figure. Locally produced cometary ions (magenta arrow), born inward of the spacecraft position w.r.t. comet, have initial velocities in the radial direction and are further accelerated along this direction by the ambipolar electric field, but also attain an anti-sunward component due to the polarization electric field. They also traverse a significant perpendicular magnetic field component, which may deflect them out of the ICA aperture plane (\mathbf{E}_{SW} should not affect these ions since that field is not actually present in the inner coma, but affect pick-up ions further upstream). In Figure 6, this is illustrated by the magenta arrow bending out below the x-y plane. (The dashed magenta line shows the projection of the magenta arrow onto the x-y plane.) The pick-up ions (yellow arrow) travel anti-sunward, with a transverse component determined primarily by upstream solar wind conditions, presumably opposite to the solar wind electric field, which can introduce a component of the motion out of the ICA detector plane, and also a transverse component in the terminator plane. Whether this results in inward or outward motion w.r.t. the comet depends on the direction of \mathbf{E}_{SW} and the clock angle of the spacecraft position. For the specific configuration in Figure 6, an \mathbf{E}_{SW} component in the positive Y direction would result in inward-streaming ions, while $\hat{\mathbf{y}} \cdot \mathbf{E}_{SW} < 0$ would give outward-flowing ions.

We have thus identified two different cometary ion populations in the inner coma, a bulk population of locally produced, predominantly radially outflowing ions and a more

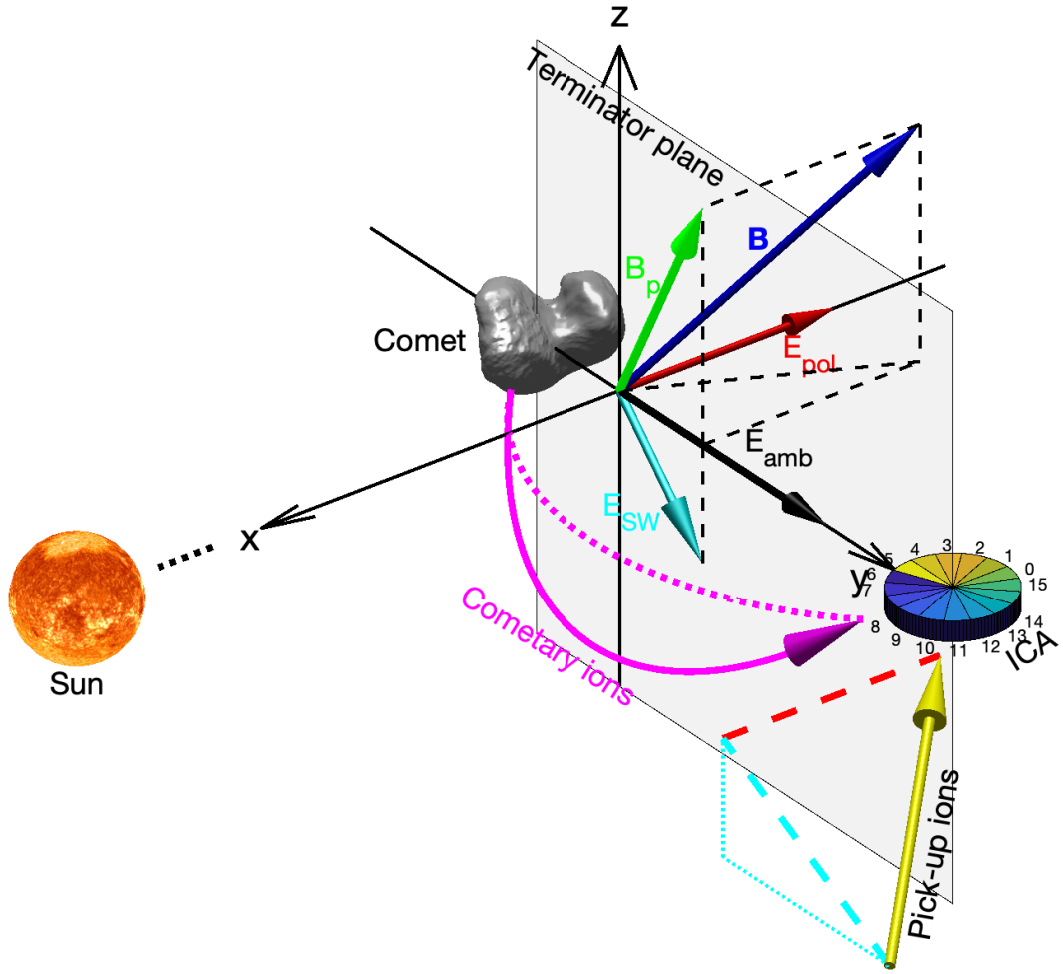


Figure 6. Schematic illustration of electric fields and ion flows in the inner coma. See text for description.

tenuous population picked up further upstream and accelerated back towards the comet by the solar wind electric field. These two populations exhibit strong relative drifts, with at least part of the relative motion across the magnetic field, and should be favorable for wave generation through the ion-ion cross-field instability. This instability is further investigated below. While some tendency towards clearer spectral peaks coincident with observations of the accelerated ions may perhaps be glanced from the results in Section 3, these two populations should in principle exist all the time in the inner coma, since there is no way to turn off the processes by which they are produced (unless some as yet unknown dynamical processes in the upstream plasma at times preclude the pick-up ions from entering the innermost region close to the nucleus). We therefore suggest that their intermittent appearance in ICA high time resolution spectra above is due to them being out of the instrument FOV a large part of the time. They may therefore be of interminable importance for wave growth in this plasma environment.

4.2 The ion-ion cross-field instability

We will restrict our analysis to the electrostatic case here; a more complete electromagnetic treatment is deferred to future work. We consider a plasma with two unmagnetized ion populations and a strongly magnetized electron population ($\omega \ll \omega_{ce}$). For dilute beams, we can neglect the electron velocity shift caused by them (Treumann & Baumjohann, 1997, Chapter 4.2). The dispersion relation then becomes:

$$0 = 1 - \frac{\omega_{pic}^2}{k^2 v_{ic}^2} Z' \left(\frac{\omega - \mathbf{k} \cdot \mathbf{V}_{ic}}{k v_{ic}} \right) - \frac{\omega_{pih}^2}{k^2 v_{ih}^2} Z' \left(\frac{\omega - \mathbf{k} \cdot \mathbf{V}_{ih}}{k v_{ih}} \right) + \frac{\omega_{pe}^2}{\omega_{ce}^2} \frac{1}{b_e} \left(1 + \frac{\omega}{k_{\parallel} v_{\parallel e}} Z \left(\frac{\omega}{k_{\parallel} v_{\parallel e}} \right) \exp(-b_e) I_0(b_e) \right) . \quad (1)$$

Here, ω_{pic} , ω_{pih} and ω_{pe} are the cold ion ("core"), hot ion ("beam") and electron plasma frequencies, respectively. v_{ic} , v_{ih} and $v_{\parallel e}$ are the thermal speeds, and \mathbf{V}_{ic} and \mathbf{V}_{ih} are the drift velocities of the ion core and beam. We also have $b_e = k_{\perp}^2 v_{\perp e}^2 / 2\omega_{ce}^2$, where ω_{ce} is the electron gyro-radius. \perp and \parallel refer to perpendicular and parallel to the magnetic field; we assume isotropic electron temperatures here, so $v_{\perp e} = v_{\parallel e}$. I_0 is the modified Bessel function of the first kind of order zero, and Z is the plasma dispersion function (Fried & Conte, 1961).

The last term in Equation 1 is the electron susceptibility χ_e . We have ignored terms of order greater than zero in the generally infinite sum over modified Bessel functions of increasing order that generally occur in this term. It is often further approximated for perpendicular propagation ($k_{\parallel} \rightarrow 0$) by using the large-argument asymptotic expansion of Z (e.g. Swanson, 2003, Appendix B) to first order, giving

$$\chi_e \approx \frac{\omega_{pe}^2}{\omega_{ce}^2} \frac{1 - \exp(-b_e) I_0(b_e)}{b_e} . \quad (2)$$

In this approximation, the wave phase velocity along the magnetic field greatly exceeds the electron thermal velocity, $\omega/k_{\parallel} \gg v_{\parallel e}$, and electrons cannot cancel charge separations in the wave electric field by flowing along the magnetic field lines. They also cannot transfer heat, so this approximation is sometimes referred to as adiabatic. With this approximation, Equation (1) reproduces Equation (5) of Graham et al. (2017).

We solve Equation (1) numerically using the MATLAB routine `fsolve` (MATLAB, 2021). The plasma dispersion function Z is evaluated numerically using a routine provided by Abrarov (2016). `fsolve` uses an iterative optimisation algorithm, minimizing the sum of squares of the components of the objective function (in our case, simply the real and imaginary parts of the right side of Equation(1)). Equation(1) has more than one solution; convergence to the branch of physical interest requires appropriate starting points. We start with the case of exactly perpendicular propagation $\psi = 90^\circ$, using Equation (2) for the electron susceptibility. For the parameters at hand, we take as

starting point $\omega_0 = 0.01$ at $k = 0.01/\rho_e$, where ρ_e is the electron gyroradius. We then use the result at each k as starting point for the next k , successively increasing k with steps of size $0.01/\rho_e$ to a maximum of $k = 2/\rho_e$. We then decrease the propagation angle slightly, first to $\psi = \arccos 10^{-6} \approx (90 - 5.73 \cdot 10^{-6})^\circ$, then gradually down to 89.42° , and use the full electron susceptibility in Equation (1), stepping through the same k values as before. At each k , we also test as starting point the previously computed solution at this k for the previous value of ψ . When the resulting solutions are different, we choose the solution whose value differs least from the value obtained at the previous k value. This has been found to work well to keep the solver on the dispersion surface of interest, when this comes close to or crosses other dispersion surfaces.

We choose as a reference case a plasma with a total density of 100 cm^{-3} , beam density, drift and thermal speeds of 10 cm^{-3} , 20 km/s and 3.5 km/s , respectively, and core drift and thermal speeds of -5 km/s and 1 km/s , respectively, where the negative sign indicates opposite direction to the beam. This corresponds well to the typical parameters we observed in Section 3. The magnetic field is set at 40 nT (although the dispersion relation is independent of magnetic field strength when the frequency and wave number are normalized to ω_{LH} and ρ_e , respectively, as long as the magnetic field doesn't vanish completely). We assume an ion mass of 18 u and a single electron population with a temperature of 10 eV .

The resulting dispersion surface is shown in Figure 7a, with the real part of the frequency on the Z axis. The surface coloring indicates the growth rate (imaginary part of the frequency) and we have also added corresponding contour plots of the growth rate on top of the dispersion surface. The maximum growth rate is just above $0.25\omega_{\text{LH}}$ and occurs for an angle of 89.86° , although almost the same growth rate is obtained also at exactly perpendicular propagation. The growth rate is high also for frequencies up to about $2\omega_{\text{LH}}$, so this covers well the range in which we typically observe elevated spectral densities in the electric field data, albeit that the exact frequency of maximum growth might be somewhat lower than where spectral peaks and plateaus tend to occur. For wave numbers $k\rho_e \gtrsim 0.86$ the dispersion surface changes abruptly at an angle of 89.76° , taking on a more ion-acoustic-like character. (This is a consequence of the wave phase velocity along the magnetic field being reduced to values comparable to the electron thermal velocity, so that the electrons can effectively cancel the wave electric field by flowing along the field lines, in contrast to the adiabatic approximation described above.) This change is discontinuous in real frequency, but continuous in the imaginary part. The contour level 0 delineates the domain of wave growth. There are unstable waves down to an angle of 89.44° . For lower angles, electron Landau damping prevails and the instability is suppressed. Wave growth is predominantly expected in the direction of the free energy, so in the direction of relative beam/core drift. We note that in Equation (1) it is the longitudinal components of the drift velocities that appear in the ion terms, so it is the drift velocity components perpendicular to the magnetic field direction that matter for this instability.

In Figures 7b–f we vary the plasma parameters from the reference case, fixing the angle of propagation to the angle of maximum growth for the reference case (89.86°). Here, the solid and dashed curves are the real and imaginary parts of the frequency, respectively, and the color of each curve gives the corresponding value of the varied parameter. The beam density (b) is gradually decreased towards zero, maintaining constant total density. The growth rate remains significant ($\gtrsim 0.1\omega_{\text{LH}}$) down to a beam density of about 1 cm^{-3} , but vanishes as the beam density is further reduced down to zero. The beam thermal velocity (c) is gradually increased, resulting in a decreasing growth rate. The instability vanishes when the thermal velocity approaches the beam drift velocity (20 km/s), thus a requirement for instability is that the cross-streaming ion beam is supersonic. This is similar to predictions from theoretical calculations on symmetric counter-streaming beams made by e.g. Davidson (1983, Chapter 3.3.7). We note that

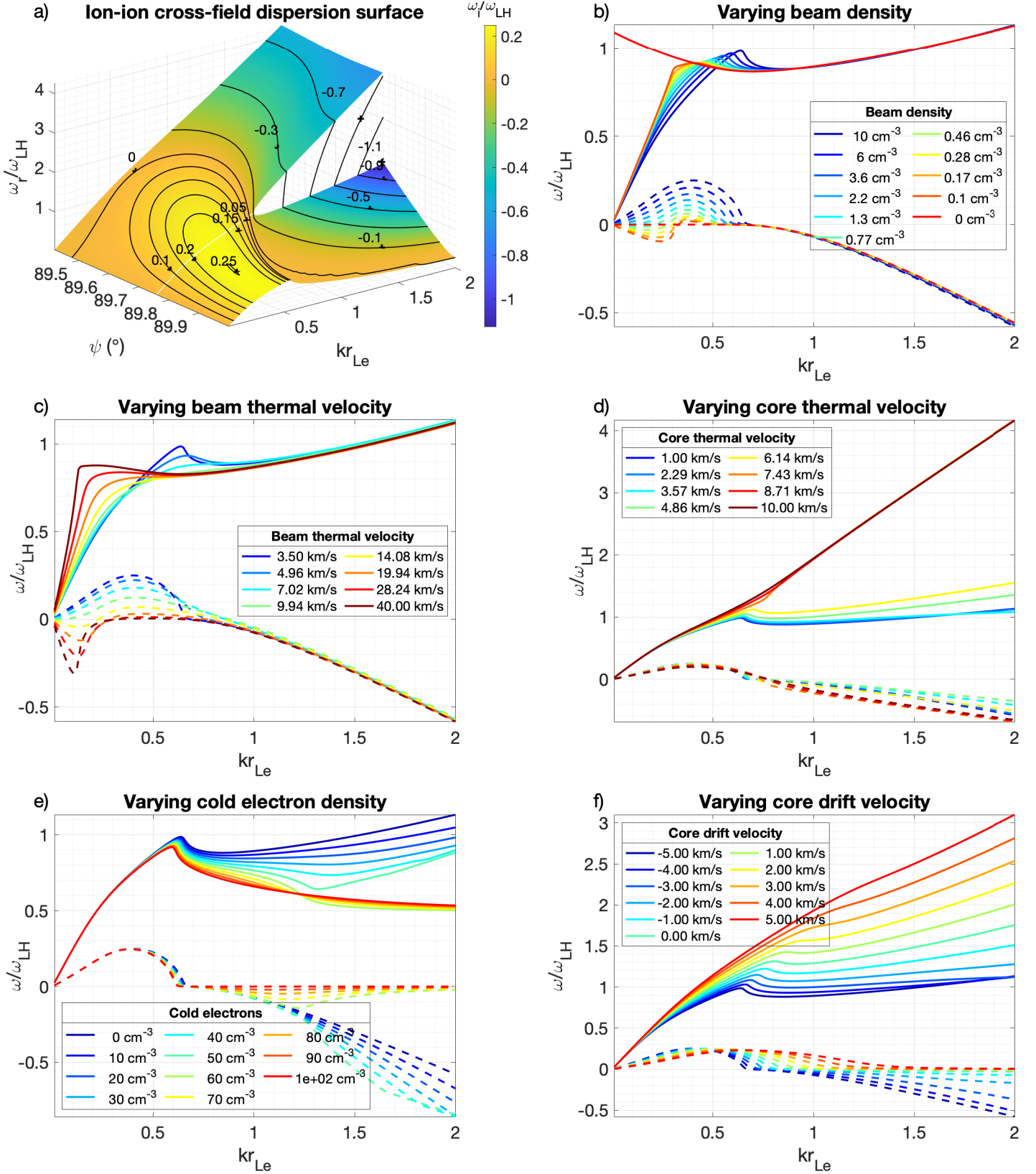


Figure 7. Numerical solutions of electrostatic dispersion relation for the ion-ion cross-field instability. **a)** Dispersion surface for the ion-ion cross-field instability, with contour lines indicating growth rate. **b–f)** Dispersion curves for varying plasma parameters for the angle of propagation of maximum growth in panel a) (89.86°). Solid and dashed lines are real and imaginary parts of the frequency, respectively.

the beams observed in Figures 2-3 and 5 are indeed supersonic. We similarly vary the thermal velocity of the ion core (d), up to twice its drift velocity. This has virtually no effect on the growing waves (although the change to ion acoustic character for larger k creeps up in angle, so that for thermal velocities $\gtrsim 8$ km/s it occurs already at angles $\psi \gtrsim 89.86^\circ$). We vary the amount of cold (0.1 eV) electrons (e) in the plasma from zero up to the total density. This also has virtually no effect on the growing waves at this angle (although some changes can be seen for k values beyond the domain of wave growth). Finally, we vary the drift velocity of the core ions (f). In the reference case, this was -5 km/s, the sign indicating opposite direction to the beam. We vary this up to a maximum of $+5$ km/s, indicating a bulk flow in the same direction as the beam (but slower). The growth rate is not much affected by this, indicating that the direction of the beam with respect to the core drift is not important for the instability. At $+5$ km/s, the relative drift speed of the two ion populations is also effectively reduced by 10 km/s; a change of this magnitude appears not to have much of an impact on the instability either. The one thing that does change is the frequency of maximum growth, which increases to values between about $(1-1.5)\omega_{\text{LH}}$ for positive core drift velocities. This is in fact closer to where spectral peaks and plateaus tend to occur in the observed electric field spectra. Overall, this instability produces significant wave growth for a wide range of parameters beyond our reference case, so it remains a good candidate for generation of lower hybrid waves also in the face of possibly large measurement errors and varying plasma conditions.

The electrostatic treatment presented here is valid in the limit $\beta_e \ll 1$. The estimated β_e for the examples shown in Figures 2–3 and 5 range from values around 0.2 to above 1, thus electromagnetic effects on the waves may be non-negligible. Wu et al. (1983) investigated such effects for overdense plasmas ($\omega_{\text{pe}} \gg \omega_{\text{ce}}$), such as we have here, finding that they generally had a stabilizing effect for large angles of propagation, close to perpendicular to the background magnetic field, but destabilizing for lower angles. The instability was thus not suppressed, but rather the propagation direction of the most unstable waves changed. Only for cross-field drift velocities V_{ih} significantly higher than the Alfvén velocity v_A was the instability suppressed by electromagnetic effects. Threshold values of V_{ih}/v_A for stability was above 2 for the largest angles of propagation, increasing rapidly to above 10 for smaller angles (Wu et al., 1983, Fig. 8). For the examples shown in Figures 2–3 and 5, the cross-field drift velocity $\langle v_i \rangle$ is often very close to v_A , and consistently stays below $2v_A$, so electromagnetic effects due to finite β_e should not prevent the growth of this instability.

5 Summary and conclusions

Electric field measurements from cometary environments are very rare, but can provide important information on how plasma waves help fashion the plasma environment. The largest set of such measurements to date was obtained by the Langmuir probe instrument onboard ESA’s Rosetta spacecraft, which followed the comet 67P/Churyumov-Gerasimenko in its orbit around the sun for over two years in 2014–2016. Here, electric field oscillations close to the local H_2O^+ lower hybrid frequency were common, and the largest amplitudes were sometimes found at or near pronounced plasma density gradients. The lower hybrid drift instability (LHDI) was thus proposed as the generation mechanism for these waves (Karlsson et al., 2017; André et al., 2017). However, the association to density gradients is not ubiquitous and other instabilities are likely contributing as well to cause the observed wave activity. In this study, we expand and build upon the previous results by considering another possible source of wave growth in the lower hybrid frequency range in the inner plasma environment of 67P; an instability due to opposite flows of streaming ions across the magnetic field.

Several previous works have shown the existence of multiple populations of cometary ions in the inner coma of 67P, distinguished by differences in energy and/or flow direction (e.g. Berčič et al., 2018; Nilsson et al., 2020). We have identified two distinct cometary

ion populations in the inner coma, a bulk population of locally produced, predominantly radially outflowing ions, and a more tenuous population picked up further upstream and accelerated back towards the comet by the solar wind electric field. These two populations exhibit strong relative drifts, and we perform an electrostatic dispersion analysis showing that conditions should be favorable for wave generation through the ion-ion cross-field instability.

The two ion populations should in principle exist all the time in the inner coma, since there is no way to turn off the processes by which they are produced (unless some as yet unknown dynamical processes in the upstream plasma at times preclude the pick-up ions from entering the innermost region close to the nucleus). They may therefore be of interminable importance for wave growth in the inner cometary plasma environment.

6 Open Research

The data used in this paper is available on the ESA Planetary Science Archive (Eriksson et al., 2020; Richter et al., 2019; Nilsson, 2021; Henri et al., 2019).

Acknowledgments

Rosetta was a European Space Agency (ESA) mission with contributions from its member states and the National Aeronautics and Space Administration (NASA). The work on RPC-LAP and RPC-ICA data was funded by the Swedish National Space Agency (SNSA) under contracts 109/12 and 108/12, the work by E. Odelstad additionally under contracts 91/17, 127/17, and Vetenskapsrådet contract 2017-0380, and S. Bergman and G. Stenberg Wieser through SNSA grants 130/16 and 96/15.

References

- Abrarov, S. (2016). *The Voigt/complex error function (second version)*. <https://www.mathworks.com/matlabcentral/fileexchange/47801-the-voigt-complex-error-function-second-version>. (MATLAB Central File Exchange)
- André, M., Odelstad, E., Graham, D. B., Eriksson, A. I., Karlsson, T., Stenberg Wieser, G., ... Richter, I. (2017, July). Lower hybrid waves at comet 67P/Churyumov-Gerasimenko. *MNRAS*, *469*, S29-S38. doi: 10.1093/mnras/stx868
- Behar, E., Nilsson, H., Alho, M., Goetz, C., & Tsurutani, B. (2017, July). The birth and growth of a solar wind cavity around a comet - Rosetta observations. *MNRAS*, *469*, S396-S403. doi: 10.1093/mnras/stx1871
- Behar, E., Nilsson, H., Wieser, G. S., Nemeth, Z., Broiles, T. W., & Richter, I. (2016, February). Mass loading at 67P/Churyumov-Gerasimenko: A case study. *Geophys. Res. Lett.*, *43*, 1411-1418. doi: 10.1002/2015GL067436
- Bergman, S., Stenberg Wieser, G., Wieser, M., Johansson, F. L., & Eriksson, A. (2020a, January). The Influence of Spacecraft Charging on Low-Energy Ion Measurements Made by RPC-ICA on Rosetta. *Journal of Geophysical Research (Space Physics)*, *125*(1), e27478. doi: 10.1029/2019JA027478
- Bergman, S., Stenberg Wieser, G., Wieser, M., Johansson, F. L., & Eriksson, A. (2020b, April). The Influence of Varying Spacecraft Potentials and Debye Lengths on In Situ Low-Energy Ion Measurements. *Journal of Geophysical Research (Space Physics)*, *125*(4), e27870. doi: 10.1029/2020JA027870
- Bergman, S., Stenberg Wieser, G., Wieser, M., Nilsson, H., Vigren, E., Beth, A., ... Eriksson, A. (2021, November). Flow directions of low-energy ions in and

- around the diamagnetic cavity of comet 67P. *MNRAS*, *507*(4), 4900-4913. doi: 10.1093/mnras/stab2470
- Berčić, L., Behar, E., Nilsson, H., Nicolaou, G., Wieser, G. S., Wieser, M., & Goetz, C. (2018, June). Cometary ion dynamics observed in the close vicinity of comet 67P/Churyumov-Gerasimenko during the intermediate activity period. *A&A*, *613*, A57. doi: 10.1051/0004-6361/201732082
- Berčić, L. (2017, May). *In-Flight Calibration of ICA - Cross-Talk Between Azimuth Sector Anodes* (Tech. Rep. No. 056). Kiruna, Sweden: Swedish Institute of Space Physics.
- Bingham, R., Dawson, J. M., & Shapiro, V. D. (2002, April). Particle acceleration by lower-hybrid turbulence. *Journal of Plasma Physics*, *68*(3), 161-172. doi: 10.1017/S0022377802001939
- Breuillard, H., Henri, P., Bucciantini, L., Volwerk, M., Karlsson, T., Eriksson, A., ... Hajra, R. (2019, October). Properties of the singing comet waves in the 67P/Churyumov-Gerasimenko plasma environment as observed by the Rosetta mission. *A&A*, *630*, A39. doi: 10.1051/0004-6361/201834876
- Broiles, T. W., Burch, J. L., Chae, K., Clark, G., Cravens, T. E., Eriksson, A., ... Samara, M. (2016, November). Statistical analysis of suprathermal electron drivers at 67P/Churyumov-Gerasimenko. *MNRAS*, *462*, S312-S322. doi: 10.1093/mnras/stw2942
- Broiles, T. W., Livadiotis, G., Burch, J. L., Chae, K., Clark, G., Cravens, T. E., ... Schwartz, S. J. (2016, August). Characterizing cometary electrons with kappa distributions. *Journal of Geophysical Research (Space Physics)*, *121*(8), 7407-7422. doi: 10.1002/2016JA022972
- Carr, C., Cupido, E., Lee, C. G. Y., Balogh, A., Beek, T., Burch, J. L., ... Trotignon, J. G. (2007, February). RPC: The Rosetta Plasma Consortium. *Space Science Reviews*, *128*, 629-647. doi: 10.1007/s11214-006-9136-4
- Clark, G., Broiles, T. W., Burch, J. L., Collinson, G. A., Cravens, T., Frahm, R. A., ... Pollock, C. J. (2015, November). Suprathermal electron environment of comet 67P/Churyumov-Gerasimenko: Observations from the Rosetta Ion and Electron Sensor. *A&A*, *583*, A24. doi: 10.1051/0004-6361/201526351
- Coates, A. J. (2004, January). Ion pickup at comets. *Advances in Space Research*, *33*, 1977-1988. doi: 10.1016/j.asr.2003.06.029
- Coroniti, F. V., Kennel, C. F., Scarf, F. L., Smith, E. J., Tsurutani, B. T., Bame, S. J., ... Wenzel, K. P. (1986, Aug). Plasma wave turbulence in the strong coupling region at comet Giacobini-Zinner. *Geophys. Res. Lett.*, *13*(8), 869-872. doi: 10.1029/GL013i008p00869
- Cravens, T. E. (1991, January). Plasma Processes in the Inner Coma. In J. Newburn R. L., M. Neugebauer, & J. Rahe (Eds.), *Iau colloq. 116: Comets in the post-halley era* (Vol. 167, p. 1211).
- Davidson, R. C. (1983, January). Kinetic waves and instabilities in a uniform plasma. In *Basic plasma physics: Selected chapters, handbook of plasma physics, volume 1* (p. 229).
- Deca, J., Henri, P., Divin, A., Eriksson, A., Galand, M., Beth, A., ... Horányi, M. (2019, August). Building a Weakly Outgassing Comet from a Generalized Ohm's Law. *Phys. Rev. Lett.*, *123*(5), 055101. doi: 10.1103/PhysRevLett.123.055101
- Edberg, N. J. T., Eriksson, A. I., Vigren, E., Johansson, F. L., Goetz, C., Nilsson, H., ... Henri, P. (2019, August). The Convective Electric Field Influence on the Cold Plasma and Diamagnetic Cavity of Comet 67P. *AJ*, *158*(2), 71. doi: 10.3847/1538-3881/ab2d28
- Eriksson, A. I., Boström, R., Gill, R., Åhlén, L., Jansson, S.-E., Wahlund, J.-E., ... Blomberg, L. G. (2007, February). RPC-LAP: The Rosetta Langmuir Probe Instrument. *Space Science Reviews*, *128*, 729-744. doi: 10.1007/s11214-006-9003-3

- Eriksson, A. I., Gill, R., Johansson, E. P. G., & Johansson, F. L. (2020). *Rosetta RPC-LAP archive of calibrated data from the COMET ESCORT 4 mission phase, RO-C-RPCLAP-3-ESC4-CALIB2-V1.0* [dataset]. <https://arcnav.psi.edu/urn:esa:psa:context:instrument:ro.rpclap>. ESA Planetary Science Archive and NASA Planetary Data System. (Identifier (LID): urn:esa:psa:context:instrument:ro.rpclap)
- Fried, B. D., & Conte, S. D. (1961). *The Plasma Dispersion Function*. New York: Academic Press.
- Galeev, A., Gringauz, K., Klimov, S., Remizov, A., Sagdeev, R., Savin, S., ... others (1988). Physical processes in the vicinity of the cometopause interpreted on the basis of plasma, magnetic field, and plasma wave data measured on board the vega 2 spacecraft. *Journal of Geophysical Research: Space Physics*, 93(A7), 7527–7531.
- Galeev, A. A. (1987, Nov). Encounters with Comets - Discoveries and Puzzles in Cometary Plasma Physics. *A&A*, 187, 12.
- Glassmeier, K.-H., Boehnhardt, H., Koschny, D., Kührt, E., & Richter, I. (2007, February). The Rosetta Mission: Flying Towards the Origin of the Solar System. *Space Science Reviews*, 128, 1-21. doi: 10.1007/s11214-006-9140-8
- Glassmeier, K.-H., Richter, I., Diedrich, A., Musmann, G., Auster, U., Motschmann, U., ... Tsurutani, B. (2007, February). RPC-MAG The Fluxgate Magnetometer in the ROSETTA Plasma Consortium. *Space Science Reviews*, 128, 649-670. doi: 10.1007/s11214-006-9114-x
- Goetz, C., Koenders, C., Hansen, K. C., Burch, J., Carr, C., Eriksson, A., ... Glassmeier, K. H. (2016, November). Structure and evolution of the diamagnetic cavity at comet 67P/Churyumov-Gerasimenko. *Monthly Notices of the Royal Astronomical Society*, 462, S459-S467. doi: 10.1093/mnras/stw3148
- Goetz, C., Koenders, C., Richter, I., Altwegg, K., Burch, J., Carr, C., ... Glassmeier, K.-H. (2016, April). First detection of a diamagnetic cavity at comet 67P/Churyumov-Gerasimenko. *Astronomy and Astrophysics*, 588, A24. doi: 10.1051/0004-6361/201527728
- Goetz, C., Plaschke, F., & Taylor, M. G. G. T. (2020). Singing comet waves in a solar wind convective electric field frame. *Earth and Space Science Open Archive*, 10. Retrieved from <https://doi.org/10.1002/essoar.10502241.1> doi: 10.1002/essoar.10502241.1
- Goldstein, R., Burch, J. L., Llera, K., Mokashi, P., Nilsson, H., Dokgo, K., ... Richter, I. (2019, October). Electron acceleration at comet 67P/Churyumov-Gerasimenko. *A&A*, 630, A40. doi: 10.1051/0004-6361/201834701
- Graham, D. B., Khotyaintsev, Y. V., Norgren, C., Vaivads, A., André, M., Toledo-Redondo, S., ... Burch, J. L. (2017, January). Lower hybrid waves in the ion diffusion and magnetospheric inflow regions. *Journal of Geophysical Research (Space Physics)*, 122(1), 517-533. doi: 10.1002/2016JA023572
- Gunell, H., Goetz, C., Eriksson, A., Nilsson, H., Simon Wedlund, C., Henri, P., ... Gibbons, A. (2017, July). Plasma waves confined to the diamagnetic cavity of comet 67P/Churyumov-Gerasimenko. *MNRAS*, 469, S84-S92. doi: 10.1093/mnras/stx1134
- Gunell, H., Nilsson, H., Hamrin, M., Eriksson, A., Odelstad, E., Maggiolo, R., ... Gibbons, A. (2017, April). Ion acoustic waves at comet 67P/Churyumov-Gerasimenko. Observations and computations. *A&A*, 600, A3. doi: 10.1051/0004-6361/201629801
- Hajra, R., Henri, P., Vallières, X., Moré, J., Gilet, N., Wattieaux, G., ... Rubin, M. (2018, April). Dynamic unmagnetized plasma in the diamagnetic cavity around comet 67P/Churyumov-Gerasimenko. *MNRAS*, 475(3), 4140-4147. doi: 10.1093/mnras/sty094
- Hansen, K. C., Altwegg, K., Berthelier, J.-J., Bieler, A., Biver, N., Bockelée-Morvan, D., ... Rosina Team (2016, November). Evolution of water production of

- 67P/Churyumov-Gerasimenko: An empirical model and a multi-instrument study. *Monthly Notices of the Royal Astronomical Society*, 462, S491-S506. doi: 10.1093/mnras/stw2413
- Henri, P., Vallières, X., Hajra, R., Goetz, C., Richter, I., Glassmeier, K.-H., ... Wattieaux, G. (2017, July). Diamagnetic region(s): structure of the unmagnetized plasma around Comet 67P/CG. *Monthly Notices of the Royal Astronomical Society*, 469, S372-S379. doi: 10.1093/mnras/stx1540
- Henri, P., Vallieres, X., Lagoutte, D., & Traore, N. (2019). *ROSETTA-ORBITER 67P RPCMIP/RPCLAP 5 ESC4 V1.0, RO-C-RPCMIP/RPCLAP-5-ESC4-V1.0* [dataset]. <https://archives.esac.esa.int/psa/ftp/INTERNATIONAL-ROSETTA-MISSION/RPCMIP/RO-C-RPCMIP-5-ESC4-V1.0/>. ESA Planetary Science Archive and NASA Planetary Data System. (Identifier (LID): urn:esa:psa:context:instrument:ro.rpcmip)
- Heritier, K. L., Henri, P., Vallières, X., Galand, M., Odelstad, E., Eriksson, A. I., ... Vigren, E. (2017, Jul). Vertical structure of the near-surface expanding ionosphere of comet 67P probed by Rosetta. *MNRAS*, 469, S118-S129. doi: 10.1093/mnras/stx1459
- Huba, J. D., & Wu, C. S. (1976, July). Effects of a magnetic field gradient on the lower hydrid drift instability. *Physics of Fluids*, 19(7), 988-994. doi: 10.1063/1.861594
- Johansson, F. L., Eriksson, A. I., Gilet, N., Henri, P., Wattieaux, G., Taylor, M. G. G. T., ... Cipriani, F. (2020, October). A charging model for the Rosetta spacecraft. *A&A*, 642, A43. doi: 10.1051/0004-6361/202038592
- Johansson, F. L., Eriksson, A. I., Vigren, E., Bucciantini, L., Henri, P., Nilsson, H., ... Odelstad, E. (2021, September). Plasma densities, flow, and solar EUV flux at comet 67P. A cross-calibration approach. *A&A*, 653, A128. doi: 10.1051/0004-6361/202039959
- Karlsson, T., Eriksson, A. I., Odelstad, E., André, M., Dickeli, G., Kullen, A., ... Richter, I. (2017, February). Rosetta measurements of lower hybrid frequency range electric field oscillations in the plasma environment of comet 67P. *Geophys. Res. Lett.*, 44, 1641-1651. doi: 10.1002/2016GL072419
- Kay, S. M. (1988). *Modern spectral estimation: theory and application*. Englewood Cliffs, N.J.: Prentice-Hall.
- Laakso, H. (1991, May). Electric fields and cold electrons in the vicinity of comet Halley. *J. Geophys. Res.*, 96(A5), 7731-7757. doi: 10.1029/90JA02459
- Madsen, B., Simon Wedlund, C., Eriksson, A., Goetz, C., Karlsson, T., Gunell, H., ... Miloch, W. J. (2018, May). Extremely Low-Frequency Waves Inside the Diamagnetic Cavity of Comet 67P/Churyumov-Gerasimenko. *Geophys. Res. Lett.*, 45(9), 3854-3864. doi: 10.1029/2017GL076415
- Masunaga, K., Nilsson, H., Behar, E., Stenberg Wieser, G., Wieser, M., & Goetz, C. (2019, October). Flow pattern of accelerated cometary ions inside and outside the diamagnetic cavity of comet 67P/Churyumov-Gerasimenko. *A&A*, 630, A43. doi: 10.1051/0004-6361/201935122
- MATLAB. (2021). *version 9.10.0.1739362 (r2021a)*. Natick, Massachusetts: The MathWorks Inc.
- Maynard, N. C. (1998, January). Electric Field Measurements in Moderate to High Density Space Plasmas with Passive Double Probes. *Washington DC American Geophysical Union Geophysical Monograph Series*, 103, 13. doi: 10.1029/GM103p0013
- Meier, P., Glassmeier, K.-H., & Motschmann, U. (2016). Modified ion-weibel instability as a possible source of wave activity at comet 67p/churyumov-gerasimenko. *Annales Geophysicae*, 34(9), 691-707. Retrieved from <https://www.ann-geophys.net/34/691/2016/> doi: 10.5194/angeo-34-691-2016
- Neugebauer, M. (1990, May). Spacecraft observations of the interaction of active comets with the solar wind. *Reviews of Geophysics*, 28(2), 231-252. doi: 10

- 993 .1029/RG028i002p00231
- 994 Nicolaou, G., Behar, E., Nilsson, H., Wieser, M., Yamauchi, M., Berčič, L., &
 995 Wieser, G. S. (2017, Jul). Energy-angle dispersion of accelerated heavy ions
 996 at 67P/Churyumov-Gerasimenko: implication in the mass-loading mechanism.
 997 *MNRAS*, *469*, S339-S345. doi: 10.1093/mnras/stx1621
- 998 Nilsson, H. (2021). *ROSETTA-ORBITER 67P RPCICA 4 ESC4 RESAMPLED*
 999 *AND CALIBRATED V1.0, RO-C-RPCICA-4-ESC4-CORR-V1.0* [dataset].
 1000 [https://pdssbn.astro.umd.edu/holdings/ro-c-rpcica-4-esc4-corr-v1](https://pdssbn.astro.umd.edu/holdings/ro-c-rpcica-4-esc4-corr-v1.0/dataset.shtml)
 1001 [.0/dataset.shtml](https://pdssbn.astro.umd.edu/holdings/ro-c-rpcica-4-esc4-corr-v1.0/dataset.shtml). ESA Planetary Science Archive and NASA Planetary
 1002 Data System. (Identifier (LID): urn:esa:psa:context:instrument:ro.rpcica)
- 1003 Nilsson, H., Gunell, H., Karlsson, T., Brenning, N., Henri, P., Goetz, C., ...
 1004 Vallières, X. (2018, August). Size of a plasma cloud matters. The polarisa-
 1005 tion electric field of a small-scale comet ionosphere. *A&A*, *616*, A50. doi:
 1006 10.1051/0004-6361/201833199
- 1007 Nilsson, H., Lundin, R., Lundin, K., Barabash, S., Borg, H., Norberg, O., ...
 1008 Burch, J. L. (2007, feb). RPC-ICA: The Ion Composition Analyzer of the
 1009 Rosetta Plasma Consortium. *Space Science Reviews*, *128*, 671-695. doi:
 1010 10.1007/s11214-006-9031-z
- 1011 Nilsson, H., Stenberg Wieser, G., Behar, E., Wedlund, C. S., Kallio, E., Gunell, H.,
 1012 ... Geiger, B. (2015, November). Evolution of the ion environment of comet
 1013 67P/Churyumov-Gerasimenko. Observations between 3.6 and 2.0 AU. *A&A*,
 1014 *583*, A20. doi: 10.1051/0004-6361/201526142
- 1015 Nilsson, H., Williamson, H., Bergman, S., Stenberg Wieser, G., Wieser, M., Behar,
 1016 E., ... Goetz, C. (2020, November). Average cometary ion flow pattern in the
 1017 vicinity of comet 67P from moment data. *MNRAS*, *498*(4), 5263-5272. doi:
 1018 10.1093/mnras/staa2613
- 1019 Odelstad, E., Eriksson, A. I., André, M., Graham, D. B., Karlsson, T., Vaivads, A.,
 1020 ... Stenberg-Wieser, G. (2020, December). Plasma Density and Magnetic
 1021 Field Fluctuations in the Ion Gyro-Frequency Range Near the Diamagnetic
 1022 Cavity of Comet 67P. *Journal of Geophysical Research (Space Physics)*,
 1023 *125*(12), e28592. doi: 10.1029/2020JA028592
- 1024 Odelstad, E., Stenberg-Wieser, G., Wieser, M., Eriksson, A. I., Nilsson, H., & Jo-
 1025 hansson, F. L. (2017, July). Measurements of the electrostatic potential
 1026 of Rosetta at comet 67P. *MNRAS*, *469*, S568-S581. doi: 10.1093/mnras/
 1027 stx2232
- 1028 Ostaszewski, K., Glassmeier, K.-H., Goetz, C., Heinisch, P., Henri, P., Park, S. A.,
 1029 ... Tsurutani, B. (2021, July). Steepening of magnetosonic waves in the inner
 1030 coma of comet 67P/Churyumov-Gerasimenko. *Annales Geophysicae*, *39*(4),
 1031 721-742. doi: 10.5194/angeo-39-721-2021
- 1032 Richter, I., Auster, H.-U., Berghofer, G., Carr, C., Cupido, E., Fornaçon, K.-H.,
 1033 ... Glassmeier, K.-H. (2016, July). Two-point observations of low-frequency
 1034 waves at 67P/Churyumov-Gerasimenko during the descent of PHILAE: com-
 1035 parison of RPCMAG and ROMAP. *Annales Geophysicae*, *34*, 609-622. doi:
 1036 10.5194/angeo-34-609-2016
- 1037 Richter, I., Glassmeier, K.-H., Goetz, C., Koenders, C., Eichelberger, H., & Cu-
 1038 pido, E. (2019). *ROSETTA-ORBITER 67P RPCMAG 4 ESC4 RE-*
 1039 *SAMPLED V9.0, RO-C-RPCMAG-4-ESC4-RESAMPLED-V9.0* [dataset].
 1040 <https://arcnav.psi.edu/urn:esa:psa:context:instrument:ro.rpcmag>.
 1041 ESA Planetary Science Archive and NASA Planetary Data System. (Identifier
 1042 (LID): urn:esa:psa:context:instrument:ro.rpcmag)
- 1043 Richter, I., Koenders, C., Auster, H.-U., Frühauff, D., Götz, C., Heinisch, P., ...
 1044 Glassmeier, K.-H. (2015, August). Observation of a new type of low-frequency
 1045 waves at comet 67P/Churyumov-Gerasimenko. *Annales Geophysicae*, *33*,
 1046 1031-1036. doi: 10.5194/angeo-33-1031-2015
- 1047 Scarf, F. L. (1989, Jan). Plasma wave observations at comets Giacobini-Zinner and

- 1048 Halley. *Washington DC American Geophysical Union Geophysical Monograph*
1049 *Series*, 53, 31-40. doi: 10.1029/GM053p0031
- 1050 Scarf, F. L., Ferdinand, V., Coroniti, V., Kennel, C. F., Gurnett, D. A., Ip, W. H.,
1051 & Smith, E. J. (1986, Apr). Plasma Wave Observations at Comet Giacobini-
1052 Zinner. *Science*, 232(4748), 377-381. doi: 10.1126/science.232.4748.377
- 1053 Stenberg Wieser, G., Odelstad, E., Wieser, M., Nilsson, H., Goetz, C., Karls-
1054 son, T., ... Gunell, H. (2017, July). Investigating short-time-scale varia-
1055 tions in cometary ions around comet 67P. *MNRAS*, 469, S522-S534. doi:
1056 10.1093/mnras/stx2133
- 1057 Swanson, D. G. (2003). *Plasma Waves, 2nd Edition*. Bristol and Philadelphia: Insti-
1058 tute of Physics Publishing. doi: 10.1201/b15744
- 1059 Taylor, M. G. G. T., Altobelli, N., Buratti, B. J., & Choukroun, M. (2017, May).
1060 The Rosetta mission orbiter science overview: the comet phase. *Philosophical*
1061 *Transactions of the Royal Society of London Series A*, 375, 20160262. doi:
1062 10.1098/rsta.2016.0262
- 1063 Thomson, D. J. (1982). Spectrum estimation and harmonic analysis. *Proceedings of*
1064 *the IEEE*, 70(9), 1055-1096.
- 1065 Treumann, R. A., & Baumjohann, W. (1997). *Advanced space plasma physics*. Lon-
1066 don: Imperial College Press. doi: 10.1142/p020
- 1067 Trotignon, J. G., Michau, J. L., Lagoutte, D., Chabassière, M., Chalumeau, G.,
1068 Colin, F., ... Zamora, P. (2007, February). RPC-MIP: the Mutual Impedance
1069 Probe of the Rosetta Plasma Consortium. *Space Science Reviews*, 128, 713-
1070 728. doi: 10.1007/s11214-006-9005-1
- 1071 Tsurutani, B. T. (1991, Jan). Comets - A laboratory for plasma waves and instabili-
1072 ties. *Washington DC American Geophysical Union Geophysical Monograph Se-*
1073 *ries*, 61, 189-209. doi: 10.1029/GM061p0189
- 1074 Tsurutani, B. T., Glassmeier, K.-H., & Neubauer, F. M. (1995, May). An in-
1075 tercomparison of plasma turbulence at three comets: Grigg-Skjellerup,
1076 Giacobini-Zinner, and Halley. *Geophys. Res. Lett.*, 22, 1149-1152. doi:
1077 10.1029/95GL00806
- 1078 Volwerk, M., Richter, I., Tsurutani, B., Götz, C., Altwegg, K., Broiles, T., ... Glass-
1079 meier, K. H. (2016, January). Mass-loading, pile-up, and mirror-mode waves at
1080 comet 67P/Churyumov-Gerasimenko. *Annales Geophysicae*, 34(1), 1-15. doi:
1081 10.5194/angeo-34-1-2016
- 1082 Williamson, H. N., Nilsson, H., Stenberg Wieser, G., Eriksson, A. I., Richter, I.,
1083 & Goetz, C. (2020, August). Momentum and Pressure Balance of a Comet
1084 Ionosphere. *Geophys. Res. Lett.*, 47(15), e88666. doi: 10.1029/2020GL088666
- 1085 Wu, C. S., Winske, D., Papadopoulos, K., Zhou, Y. M., Tsai, S. T., & Guo, S. C.
1086 (1983, May). A kinetic cross-field streaming instability. *Physics of Fluids*,
1087 26(5), 1259-1267. doi: 10.1063/1.864285